Poroelastic Modeling of Groundwater and Hydrocarbon Reservoirs: Investigating the Effects of Fluid Extraction on Fault Stability

by

Anna Louise Rogers

B.S. Hons. Major in Physics, Arts Minor in Geological Sciences, Queen's University, 2014

Submitted to the Department of
Earth, Atmospheric and Planetary Sciences
in partial fulfillment of the requirements for the degree of

Master of Science in Geophysics

at the

MASSACHUSETTS INSTITUTE OF TECHNOLOGY

September 2017

Author ...... Signature redacted ....
Department of
Earth, Atmospheric and Planetary Sciences
August 11, 2017

Certified by.... Signature redacted ....
Bradford H. Hager
Cecil and Ida Green Professor of Earth Sciences
Director of the Earth Resources Laboratory
Thesis Supervisor

Accepted by .... Signature redacted ....
Robert D. Van der Hilst
Schlumberger Professor of Earth Sciences
Head of the Department of Earth, Atmospheric and Planetary Sciences

Poroelastic Modeling of Groundwater and Hydrocarbon Reservoirs: Investigating the Effects of Fluid Extraction on Fault Stability

by

Anna Louise Rogers

Submitted to the Department of
Earth, Atmospheric and Planetary Sciences
on August 11, 2017, in partial fulfillment of the
requirements for the degree of
Master of Science in Geophysics

Abstract

The possibility of human-triggered earthquakes is critical to understand for hazard mitigation. This project was developed to better understand the stability of faults in areas with high amounts of fluid extraction, and was applied to both a groundwater and hydrocarbon basin. The theory of poroelasticity was used to calculate the stress changes resulting from fluid flow. Then, the resulting fault stability was evaluated with the the Coulomb Failure Function (ΔCFF). A COMSOL and MATLAB workflow was used to derive the results.

Two applications were completed. The primary research focused on the extraction from a groundwater aquifer in Lorca, Spain, in relation to the M_w 5.1, 2011 earthquake. A smaller project was completed for the production of an oil well in Wheeler Ridge, California, in relation to the M_w 7.7, 1952 earthquake.

In Lorca, it was found that extraction from a local aquifer promoted failure on an antithetic fault to the major Alhama de Murcia Fault. Specifically, while the left-lateral portion of the slip was stabilized, the reverse component of the slip was promoted (depth $\sim$5 km). Published InSAR and focal mechanism results support a rupture plane aligned with the antithetic fault. The final stress change was $\approx$0.03 MPa which is small but not negligible compared to the expected total stress drop ($\approx$2 MPa).

In California, the production from Well 85-29 was of interest. It was found that oil extraction promoted failure on the White Wolf Fault. There was a region adjacent to but below the reservoir that tended toward destabilization after the production. However, there was a notably small stress change ($\approx$0.5 kPA).

This project lends to some important conclusions, and demonstrates that the poroelastic deformation of an aquifer or reservoir can result in distinct zones of stabilization and destabilization on pre-existing faults.

Thesis Supervisor: Bradford H. Hager
Title: Cecil and Ida Green Professor of Earth Sciences
Director of the Earth Resources Laboratory

Contents

List of Figures

List of Tables

Chapter 1

Introduction

1.1 Motivation

The primary objective of this project was to evaluate the stability of pre-existing faults adjacent to regions with high volumes of fluid extraction. To better understand subsurface stress changes resulting from fluid flow, the theory of poroelasticity was applied. Then, the Coulomb Failure Function (ΔCFF) was used to evaluate the stability of a fault resulting from these stress changes. The research focused on two earthquakes; the 2011 Lorca, Spain Earthquake and the 1952 Wheeler Ridge (Kern County), California Earthquake. If it is found that fluid extraction can push a fault toward instability, this could have implications on the possibility of earthquakes triggered by human activity.

Poroelasticity is an important phenomenon in natural processes, and dictates the time-dependent relationship between subsurface stress changes and fluid flow. The effect can be seen in numerous examples in earth sciences, but due to the difficulty and expense of the numerical computations it is often not included in applied models. This project proposes a straight forward way to integrate COMSOL and MATLAB to calculate the stress changes caused by fluid extraction. Due to the ease of use and relative availability of both these programs, this proposed workflow could allow poroelasticity to be applied in more projects.

1.2 Project Overview

The COMSOL-MATLAB workflow was applied to two projects: Lorca, Spain and Wheeler Ridge, California. Both areas have a history of seismic activity. The Lorca project was more involved than the Wheeler Ridge section, and the goals of this project were three-fold. First, it was attempted to validate the poroelastic COMSOL and MATLAB workflow by comparing it to a simplified Coulomb 3.4 Model. Coulomb 3.4 is a widely accepted and implemented USGS code, and is assumed to be reliable for simplified scenarios. Additionally, with a smaller focus, the results from the poroelastic model were compared to an elastic model. The elastic model is different in that it doesn't fully apply the fluid flow equations in the model. It was found that the application of poroelasticity significantly changed the results, and suggested that it should be considered when analyzing the stress changes from fluid extraction.

Once the workflow had been applied to Lorca, Spain and compared to Coulomb 3.4, the method was deemed to be reliable. The workflow was then applied to Wheeler Ridge, California. For both locations, the subsurface stress changes due to the fluid extraction were analyzed.

1.3 Introduction to the Theory

1.3.1 Poroelasticity

Poroelasticity describes a coupled reaction between fluids and deformation of porous solids. The theory dictates how fluid extraction produces stress changes in isotropic, saturated rocks. It also explains how stresses applied to an aquifer can affect fluid pressure and thus water level changes. These two phenomena are an example of a coupled problem, and leads to interesting feedback mechanisms [1].

Before the coupling is described, the concept of effective stress will described. A soil or rock can be thought of as a skeleton of solid particles, which contains continuous and connected voids that are fully saturated with fluid. The concept of effective stress described a balance between the total normal stress, soil skeleton effective normal stress and pore fluid pressure. In simple terms, the total normal stress (σ_n) represents the load caused by any mass, or applied stress, above the zone of interest. The total normal stress must be balanced by the stress within the subsurface pore fluid and by the skeleton of the rock. This balance can be seen in Figure 1-1 and Equation 1.1.

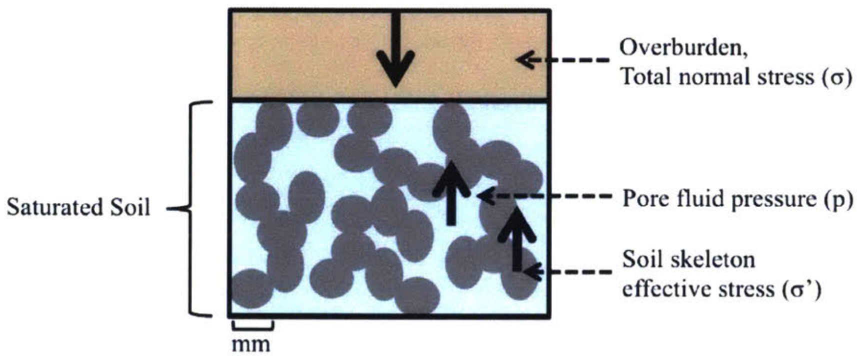

Figure 1-1: Effective Stress in a Porous Media

$$|\sigma_n| = |\sigma_n^{'}| + |\alpha p_f| \tag{1.1}$$

The effective normal stress $\sigma_n^{'}$ represents the stress transmitted through the soil skeleton only. The pore fluid pressure p_f is the pressure of the fluids within the interconnected voids. The Biot-Willis coefficient (α) dictates the proportion of fluid pressure that balances the overburden stress. With the assumption that the overburden stress stays constant throughout time, there is a trade off between the pore fluid pressure and the effective normal stress. Overburden normal forces can either be resisted directly by the soil skeleton, or can be supported by the fluid in the voids. Conversely, shear stresses are independent of the pore fluid pressure and they are only distributed within the soil skeleton.

Now, the coupling mechanisms will be described. The first type of coupling is *fluid to solid*, where a change in fluid pressure or fluid mass produces a change in the volume of the porous medium. The change in volume results in a change in stress and strain of the solid. One example of this is the long term removal of groundwater. The extraction of water causes the volume of the porous material to decrease, and the land to subside. This is commonly seen in the California Central Valley area. Additionally, this has been seen in an oil field in Goose Creek, Texas. 100 million barrels of oil were extracted, and led to substantial subsidence of the land [1]. Conversely, an opposite effect can be seen in areas with heavy rainfall. The input of fluid into the porous medium causes the expansion of the porous material, causing the land to bulge [2]. These are two standard examples of fluid to solid coupling, and demonstrates that this is a definite and observable effect in nature.

The second type of coupling is *solid to fluid*, where a change in applied stress produces a change in fluid pressure. In an early study done in Wisconsin [1], it was reported that as a train approached the station, the aquifer was compressed, and the water pressure increased. As the train departed the station, the aquifer expanded and the water pressure decreased [1]. This is an example of where solid to fluid coupling can be seen in nature and indicates that it is important to consider.

The importance of the coupling should be emphasized, and poroelasticity can be compared to thermoelasticity. Both theories share very similar equations and framework, however, thermoelasticity is dominantly uncoupled. Consider the heat to solid coupling of a material. Heating of a solid causes a stress change, and can have a considerable effect. However, with solid to heating coupling, applying a stress or strain to a material does not cause a significant change in heat. Within the frame work of fluid flow, the elastic model can be considered to be analogous uncoupled model. It assumes that there is solid to fluid coupling, but no fluid to solid coupling. This makes it a simpler model compared to poroelasticity. In this project, the elastic results will be compared with the poroelastic results. It is found that the full coupling is an important aspect to consider. The governing equations for elasticity and poroelasticity will be described in Chapter 3.

1.3.2 Gravitational Unloading Stresses

In addition to poroelasticity, an important effect to consider is the gravitational unloading stress. As the water is extracted from the aquifer, a significant portion of mass is removed and the density decreases. Thus, the removal of water leads to an upward change in stress on the region near the aquifer, as seen in Figure 1-2. The stress change is approximated as a boundary load, since it is assumed that the depth being affected by water removal is small compared to the total depth of the aquifer. It should be noted that this effect is the only resulting stress from groundwater extraction that is considered in the elastic model.

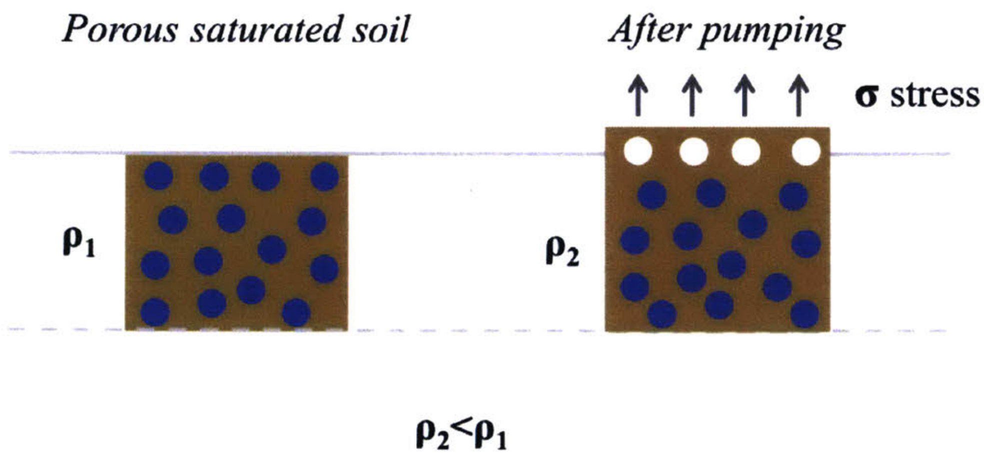

Figure 1-2: Gravitational Unloading Stresses

1.3.3 Stress Conventions

For this project, the continuum mechanics definition of stress will be used. Compressive stress is negative and extensional stress is positive. The 3D stress tensor is symmetric and the following variable convention is used.

$$\boldsymbol{\sigma} = \begin{bmatrix} \sigma_{xx} & \sigma_{xy} & \sigma_{xz} \\ \sigma_{xy} & \sigma_{yy} & \sigma_{yz} \\ \sigma_{xz} & \sigma_{yz} & \sigma_{zz} \end{bmatrix} \tag{1.2}$$

In the case of normal and shear stresses specific for a plane, the variables σ_n and τ will be used. To describe the fault slip, the Aki-Richards convention will be used, as seen in Figure 1-3 [3].

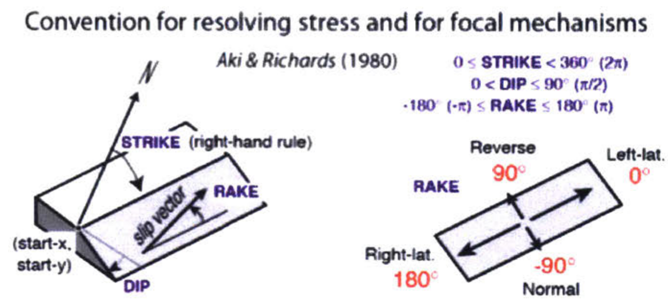

Figure 1-3: Aki and Richards Fault Convention from the Coulomb 3.4 Manual

1.4 Introduction to the Projects

1.4.1 Lorca, Spain

On May 11, 2011 a M_w 5.1 earthquake occurred in Lorca, Spain. Significant destruction occurred in the city, with damage on 1164 buildings and losses estimated at 1200 M€. The earthquake claimed nine lives and caused over 300 injuries [4]. Although the 2011 earthquake was particularily damaging, the region is considered to be an area of high seismic risk in Spain with three recent M_W 4.8, 5.0, and 4.8 earthquakes occuring in 1999, 2002 and 2005 respectively [5]. Lorca is located in southeastern Spain along a segment of a major plate boundary. There is an approximate northwest-southeast convergence motion which results in a series of complex thrusting and strike-slip faults. However, the shallow slip of the May 2011 earthquake was uncharacteristic for the region and it has been suggested that the earthquake was triggered by groundwater extraction from a nearby aquifer [6] [7]. The city, fault and aquifer are shown in Figure 1-4.

The Alto Guadalentín Basin has shown high subsidence rates due to long term groundwater pumping. Groundwater table levels are available at a minimal number

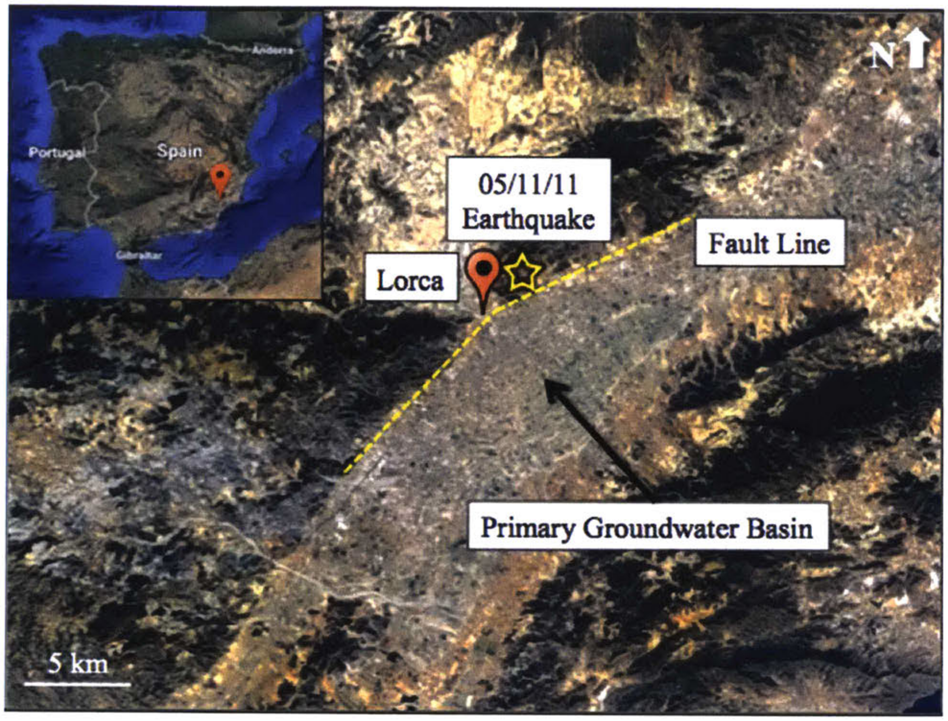

Figure 1-4: Lorca, Spain with Major Fault and Groundwater Basin, from Google Earth

of wells but indicate a water table level change of 250m from 1960 - 2010, indicating a change in approximately 5m/year. Previous research by González *et al.* applied a purely elastic model, and suggested the earthquake was triggered by gravitational unloading induced by groundwater depletion [6] [7]. Alternatively, this project introduces fluid flow and considers the role of poroelasticity. This section of the project was compared to the poroelastic results by Jha *et al.* [8] [9] [10].

An additional noteworthy feature of this earthquake is the ambiguity of the ruptured fault plane. Initial moment tensor solutions suggest that the slip could have occurred on one of two fault planes. The first set of results supports a plane that strikes approximately N230°E and dips NW, which is aligned with the major Alhama de Murcia Fault (AMF) fault. The second set suggests a plane that strikes approximately N50°E and dips SW. It has been proposed that this is aligned with an unidentified antithetic fault, which will be referred to as the UAF [8]. This project will explore if either of these faults would have been more likely to fail from the long term water extraction. However, it is important to note that the focal mechanisms from the 2011 earthquake are generally aligned with the expected rupture patterns from the area. This indicates that the 2011 rupture was primarily tectonically driven. If the stress changes caused by pumping are found to be significant, then the extraction may have helped to trigger an earthquake on a pre-existing fault, but it did not induce an earthquake in a seismically inactive area.

The Lorca, Spain section of this project was developed to be able to draw on the work of others and compare the results. Both González *et al.* and Jha *et al.* completed work on this earthquake, but with differing approaches. These will be described further in Chapter 2.

1.4.2 Wheeler Ridge, California

The Wheeler Ridge Oil field is located in the Bakersfield region of California. The field is located in the foothills of the San Emigdio Mountains, 25 miles south of the city of Bakersfield. The possibility for oil was recognized in 1910 and the first successful well was drilled in 1922. The first producing well was drilled to a depth of 2185 ft and had an initial production of 275 bbl/day. The original field is referred to as the Old Area and 41 wells were drilled here. Later, in 1947-1950, the Coal Oil Canyon Area was discovered and developed. This development targeted the Santa Margarita formation between 848 - 1176 ft (upper Miocene). The first well had a production of 165 bbl/day. A subsequent 23 wells were drilled here. By June 30 1951, a total of 5.3×10^6 barrels had been produced [11].

Later, in April 1951, a discovery was made in the area in well KCLD 85-29. The target was the Eocene interval from 9,600 ft -9,756 ft. The production began in May 1952, and initally flowed at a substantial volume of 1,170 bbl/day but leveled out to 400 bbl/day. In mid-1952, this was the only production well at that depth [12].

On July 21, 1952, a significant earthquake occurred on the White Wolf Fault. The earthquake had a magnitude of M_w 7.7 on the Richter Scale and was devastating to the area. The depth and location of the earthquake are relatively unconstrained due to the lack of data during that time period. The original records at the California

Institute of Technology suggested the earthquake originated at a depth of 10 miles and at a location of 35° 00' N, 19° 02' W, in the Wheeler Ridge region along the White Wolf Fault. However, these locations and depths are imprecise and are not seriously considered in the evaluation. The known parameters are shown in Figure 1-5. The calculations from seismology indicate that the fault is steeply dipping (60°-66°) toward the SE. The primary movement of the fault was reverse with a lesser left lateral component. Although the fault was known to have movement in late geologic time, it was not considered to be a threat [13].

Due to the unpredicted slip on this fault, it has been proposed that the poroelastic stress change from the oil production initiated the rupture. The focus of the study will be on the KCLD 85-29 well from the 1952 discovery and production.

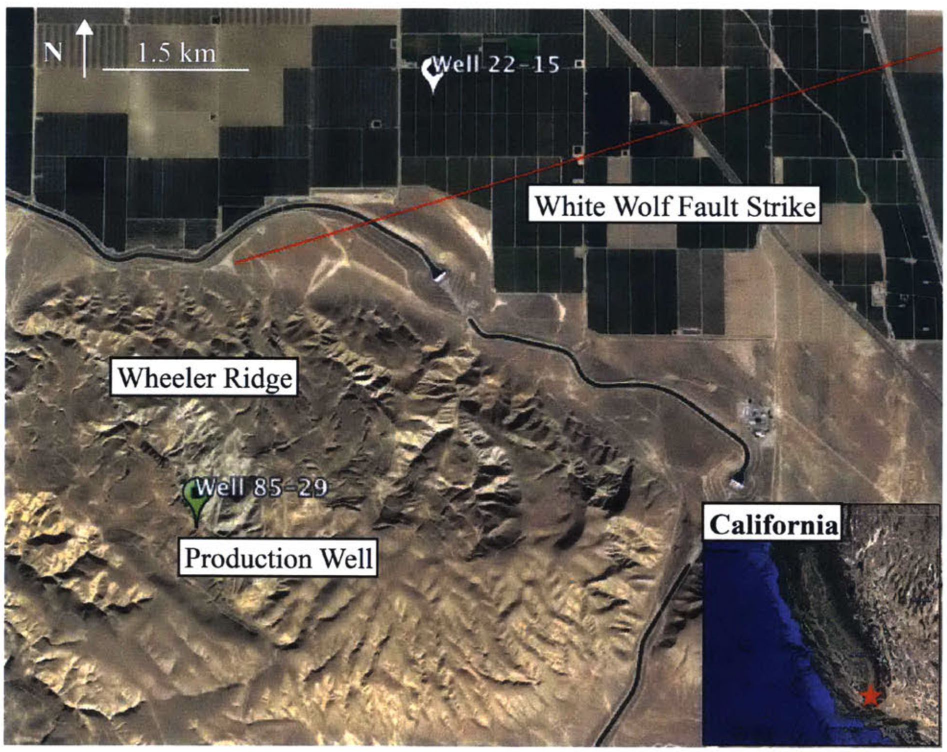

Figure 1-5: Wheeler Ridge with Major Fault and Production Well, from Google Earth

Chapter 2

Literature Review

This chapter will be used to summarize the important research regarding the Lorca earthquake. First, the geology of the area will be explored in the Martínez-Díaz *et al.* 2012 [4] paper. The specifics of the nearby aquifer (Alto Guadalentín Basin) will be covered using work from González and Fernández [14]. Next, the 2011 Lorca earthquake will be looked at in more detail by considering the directivity, moment tensor inversions and InSAR data in papers by López-Comino *et al.* 2012 [5], Michelle *et al.* 2013 [15] and Pro *et al.* 2014 [16]. Finally, the research specific to the pumping of water and triggering of the earthquake done by Jha *et al.* 2013 [8] [9] [10] and Gonzalez *et al.* 2012 [6] [7] will be explored.

2.1 Active Tectonics of the Alhama de Murcia Fault

Martínez-Díaz *et al.* provide an overview of the geology of Lorca, Spain. The Alhama De Murcia Fault (AMF) has been identified as a region with a complex distribution of stress. The area traditionally has strike-slip and oblique slip (reverse-sinistral) movements, due to large-scale NNW-SSE shortening direction trends of south-east Spain. There are four structural segments within the main fault zone. The segment of interest for this project is the Lorca-Totana section. In this section, the direction of the main fault zone varies from N 38° to N 60°, indicating that there is a prominent curve within the fault. The main fault zone is shown in Figure 2-1.

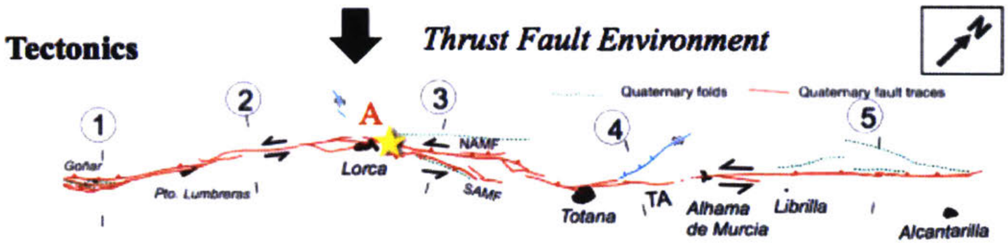

Figure 2-1: Martínez-Díaz *et al.* AMF Depiction with Annotations

The dip of the main fault is consistent with a range from 60° to 70°. However, within the segment of interest there are also branches which show several antithetic faults. These antithetic faults are generally not understood. The authors state that they believe the antithetic faults exist, but their formation is still under debate. A depiction of the faults by cross section are shown in Figure 2-2, however the location and dip of the unidentified antithetic faults (UAF) are not truly known.

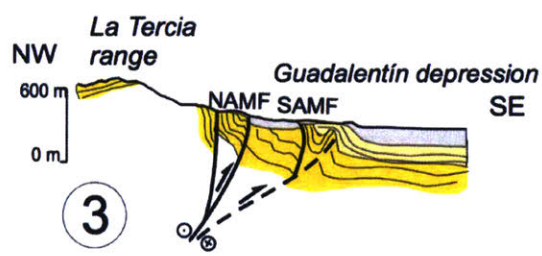

Figure 2-2: Martínez-Díaz *et al.* Fault Cross Section

Martínez-Díaz *et al.* also explored the 2011 earthquake specifically. From field work completed immediately after the earthquake, it was concluded that there was no surface rupture. The focal mechanisms were investigated and they suggested a plane that was sub parallel to the AMF, dipping to the north. The aftershocks were relocated by López-Comino *et al.* and they were found to be concentrated to the north of the inter-segment zone. This suggests that the source of the earthquake was a fault parallel and to the north of the AMF. Martínez-Díaz *et al.* interpret the source to be on a fault to the north and dipping north. They draw this conclusion from a preliminary study completed by Vissers and Meijninjer (2011).

2.2 Alto Guadalentín Basin Aquifer Compaction

González and Fernández applied satellite differential radar interferometry (DInSAR) to estimate the aquifer properties of the Guadalentín Basin in south east Spain. This area has shown the highest recorded rates of groundwater related land subsidence in Europe (>10 cm/yr).

The valley containing the Guadalentín Basin is relatively flat, with a series of alluvial fans. The primary basin consists of two sub-basins, the Alto and Bajo. The focus of this study will be the Alto Guadalentín Basin. The basement of the aquifer is composed of a relatively impermeable metamorphic complex, overlain by a permeable conglomerate or calcarenite series. The very top is a lower permeability layer of sand, silt, clays and compressible conglomerates. The basin borders are controlled by the major fault zones in the area.

In the past, the water levels were near the land surface. Increased exploitation began in 1960-1970 and by 1987 it was legally declared to be provisionally overexploited. Over the years, 1000 wells were used for pumping with rates increasing from 24 hm^3/year in 1978 to 86 hm^3/year in 2006. This resulted in a water level drop between 0.5-10 m/yr, depending on the location in the aquifer.

After analysis of the SAR data, it was concluded that most of the deformation is due to inelastic and non recoverable compaction of the aquitard. The maximum subsidence was seen in the middle of the aquifer, with decreasing contours radiating outwards. Since the compaction was deemed to be non-linear, and there is no data for the beginning of extraction, it is difficult to estimate the total amount of compaction in the Alto Guadalentín Basin since pumping began in 1960. However, González and Fernández measure the cumulative to be $\sim$2 m from 1990-2010, which indicates that the total subsidence rate could be up to 10 cm/yr.

2.3 Rupture Directivity of the Lorca Earthquake

López-Comino *et al.* focused on analyzing seismograms to characterize the source of the earthquake. They completed a moment tensor inversion, hypocenter relocation and a directivity study.

From the moment tensor inversion, a strike of N240°E, dip 54°, rake 44° and a depth between 4-6 km was obtained. Moment tensor solutions for previous earthquakes in SE Spain indicate mostly strike slip faulting [17]. This is consistent with the overall left lateral motion of the NE-SW trending area known as the Beltic-Alboran Shear Zone [18]. However, depending on the orientation of the plane, other earthquakes have been known to have reverse and normal faulting, so left lateral motion is not exclusive to the area. The moment tensor mechanisms for the M_w 5.2 mainshock, M_w 4.6 foreshock and M_w 3.9 aftershock are shown in Figure 2-3.

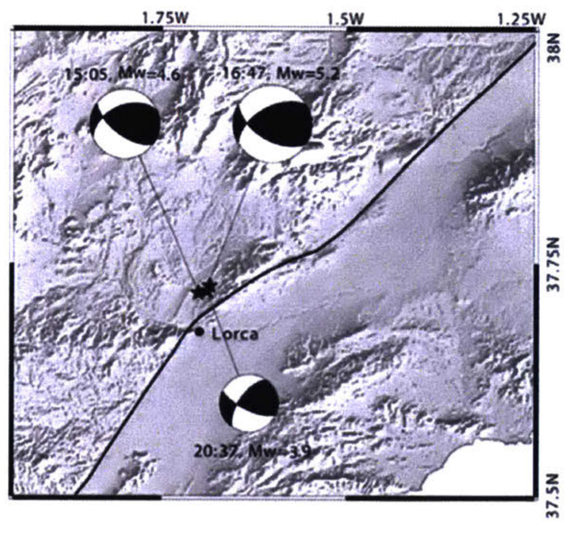

Figure 2-3: López-Comino *et al.* Moment Tensors Mechanisms

Next, a hypocenter relocation was performed. From this, the location and strike of the epicenter agrees well with the AMF to the NW of Lorca. The mainshock hypocenter is in the NE end of the segment, and this suggests that the rupture propagated from NE to SW. The location of the mainshock was determined to be 37.727°N, 1.686°W and 4.6 km depth. The fault slip calculated from the aftershock relocations was 4 km.

The directivity effect was also pronounced in this area. Apparent durations were modeled assuming a line source. The direct P and S waves mainly carry the information on the horizontal rupture propagation. After modeling the general case of an asymmetric bilateral line source, it was found that the directivity was N209°E for the S-waves and N231°E for the P-waves, with an average directivity of N220°E. This does not perfectly match the fault strike of N240°E strike since it does not include the up-dip component of the slip. This indicates that there was a definite reverse portion of the slip.

2.4 InSAR Results of the Lorca Earthquake

Michelle *et al.* used space geodetic techniques to map the displacement field of the Lorca, Spain earthquake. The interferometric synthetic aperture radar (InSAR) signal was analyzed. For the analysis, the data from the European C-band Advanced SAR (ASAR) sensor on the Environmental Satellite (ENVISAT) was used. An elastic dislocation model was used to characterize the fault plane geometry.

It was found that there were two solutions that were consistent with the InSAR signals. This is in agreement with the cited literature, where two different fault planes have been found to agree with moment tensor inversions. The first solutions is from the Spanish Instituto Geografico Nacional (IGN), the Istituto Andaluz de Geofisica (IAG), the Global Centroid Moment Tensor solution (GCMT) and the University of Nice (Geoazur). They are consistent with a fault with a strike N245°E and dip 45°. This solution would be consistent with slip on a segment of the main AMF fault. Alternatively, the Italian Instituto Nazionale di Geofisica e Vulcanologia (INGV), the German Geo Forschungs Zentrum (GFZ) and the US Geological Survey (USGS) support a fault with a strike of N50°E and dip 50°. This solution is consistent with slip on the blind thrust fault (UAF).

Both models are likely from the InSAR results, and it was found that the true fault plane could not be discriminated. There were challenges in the area due to the subsidence of the local aquifer. As mentioned before, the region near the aquifer had been undergoing rapid subsidence due to the extensive pumping of water. Complexities arose when trying to separate the InSAR signals due to the earthquake and to those from pumping. Other issues stemmed from the blind seismic rupture and the noise level in the interferogram stack. Therefore, both of the following rupture planes listed in Table 2.1 are options for the 2011 Lorca Earthquake

Table 2.1: Michelle *et al.* Fault Plane Model Parameters from InSAR

Dip (°)	**Strike**	**Rake** (°)	**Depth** (km)	**Slip** (mm^3)	**Fault Analogue**
45	N245°E	77	3.2	210 R 65 LL	AMF
50	N50°E	77	2.8	210 R 60 LL	UAF

Note that the rake is larger than what is seen in other studies. This could be attributed to the fact that the InSAR data is particularly sensitive to the vertical component of the movement.

2.5 Rupture Process of the Lorca Earthquake

C. Pro *et al.* completed a study of the rupture process of the Lorca Earthquake from an inversion of body waves at regional and teleseismic distances. They obtained a bilateral rupture with 27 cm slip, propagating WSW, with a strike of N238°E, dip 54° and rake 59°. They proposed that the ruptured fault plane was the Cejo de los Enamorados Fault (CEF), which has the same orientation as and is parallel to the AMF, but is located ~N of Lorca. They argued that the epicenter of the earthquake falls 4 km to the west of the main line of the AMF, and that the foreshock, main shock and aftershocks correspond directly with the CEF. Note that the CEF is not equivalent to the UAF described above, since the dip direction is opposite.

The authors allude to the issue that there is a general disagreement on the complexities of the AMF and adjacent faults, and there is not an accepted geological structure of the area.

2.6 Research by González *et al.*

Previous research on the link between groundwater extraction and the 2011 Lorca Earthquake was completed by González *et al.* For the study, the authors began by determining the seismic slip, using surface deformation and GPS data. An elastic dislocation model was used to show that earthquake nucleation occurred at a shallow depth of 2-4 km along the AMF. The best fitting dislocation model suggested a reverse and left lateral slip fault striking N230E and dipping 70° to the NE. It was determined that the area of fault slip correlated well with the pattern of positive Coulomb Stress change (ΔCFF) that was calculated to result from the gravitational unloading by groundwater extraction from the nearby basin. The concept of ΔCFF will be described further in Chapter 3, but a positive ΔCFF indicates destabilization while a negative ΔCFF suggests stabilization.

For the ΔCFF calculation, Gonzalez *et al.* only considered the stress change induced by the 'crustal (un-)loading' of the near surface mass, and not poroelasticity. They modified parameters including the aquifer areal shape, aquifer porosities, slip rake, the role of pore pressure diffusion and fault friction. In the final model, a fault rake of 36°, porosity of 5%, fault friction of 0.5 and Skempton coefficient of 0.6 was assumed. However, as mentioned, the pore pressure diffusion was concluded to be insignificant over the modeled time-scales and it was not included in the model. The hydraulic head trends and ground subsidence trends that were used for analysis are shown in Figure 2-4. It was seen that the hydraulic head drop was approximately 6.8 m/yr and the subsidence was 10 cm/yr. An average hydraulic head drop of 5 m/yr was assumed.

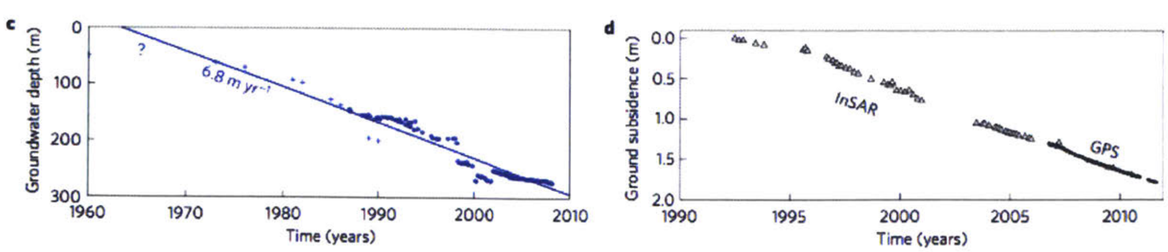

Figure 2-4: González *et al.* Field Hydraulic Head and Subsidence Trends

Gonzalez *et al.* concluded that the slip distribution of the earthquake was controlled by gravitational unloading from groundwater extraction. It was proposed that the earthquake is tectonically driven, but that the groundwater stress changes promoted failure at a certain nucleation point. This is a significant conclusion, and states that the 2011 Lorca Earthquake was triggered by anthropogenic activity.

2.7 Research by Jha *et al.*

Jha *et al.* also investigated the role of fluid extraction in the triggering of the Lorca Earthquake. However, the approach was different than González *et al.* in a few significant ways. Primarily, the role of fluid pressure was included in the calculations and a poroelastic model was assumed. Additionally, Jha *et al.* considered the ambiguity in the location of the actual rupture plane, and discussed the two equivalent fault plane solutions. It was concluded that the geometry and position of the actual rupture plane is uncertain, and consequently both a northwest dipping plane (AMF) and a southwest dipping plane (UAF) was modeled. Jha *et al.* also calculated the approximate stress drop for this earthquake to be $\approx$2 MPa.

From considering pore fluid pressure, the groundwater extraction leads to both a decrease in the weight of the overlying rock, and a volumetric contraction of the aquifer. In contrast, this volumetric contraction was not considered in the Model by González *et al.* Jha *et al.* considered a fully coupled model and proposed that fluid pressure is a significant effect in the sensitivity of the ΔCFF. Two models were created; one for the AMF and one for the UAF.

2.7.1 Model Parameters

Using CUBIT, Jha *et al.* constructed a 20 km X 20 km x 10 km 3D model, rotated with the x-axis parallel to a segment of the AMF fault. The high permeability aquifer was assumed to be $\sim$500 m thick and is underlain by low permeability basement rock. A two phase flow model was considered, with air and water. Jha *et al.* created the model so that as the water table dropped from the pumping wells, the water in the pores was replaced with air. However, since the specific contribution from air was not considered for this project, the gas parameters will not be discussed further. The constants used in Jha *et al.*'s model are shown in Table 2.2.

Table 2.2: Jha *et al.*'s Model Constants

Poisson's Ratio	ν	0.25
Biot Coefficient	α	1
Porosity	θ	0.1
Solid Density	ρ_s	2600 [kg/m^3]
Density of Water	ρ_w	1000 [kg/m^3]
Density of the Body	ρ_b	$(1-\theta)\rho_s + \theta\rho_w$
Coefficient of Friction	μ	0.47
AMF Dip	θ_{AMF}	54°
UAF Dip	θ_{UAF}	50°

The aquifer is confined by the impermeable fault, and the adjacent grid boundaries. The permeability and Young's Modulus were based off of empirical relationships and varied with depth. However, the functions displayed in the poster and thesis were not consistent so the exact formulae are not provided here. However, the functions could be generalized and the trends are shown in Table 2.3. The displayed log permeability equation only applies to the basin region, and the outside permeability was constant and very low. The Young's Modulus function applies everywhere in the model.

The initial conditions for Jha *et al.*'s model are shown in Table 2.4. Note that positive z points up, and u, v, w are the displacements in the x, y, z directions respectively. Standard boundary conditions were used in the model. To replicate the thrust fault environment, a normal compression was applied at $y+$, or the mountain side of the fault. A free condition was applied to the top surface ($z+$) and a Roller condition was applied to all other sides ($x+$, x-, z-, y-). Additionally, a no flux boundary condition was applied on all sides.

Table 2.3: Jha *et al.*'s Model Young's Modulus and Permeability

Young's Modulus	**Permeability**
100 [MPa] at z=0 [m]	1000 [mD] at z=0 [m]
80 [GPa] at z=-10^4 [m]	$\approx$ 0 [mD] at z=-10^3 [m]
·Approximately linear relationship	· Approximately log relationship in the basin, constant (k_r=0.0001 [mD]) outside

Table 2.4: Jha *et al.*'s Model Initial Conditions

Stress in z direction	σ_{zz}	-$\rho_b g\|z\|$
Stress in x direction	σ_{xx}	-1.5$\rho_b g\|z\|$
Stress in y direction	σ_{yy}	-2$\rho_b g\|z\|$
Pore Pressure	p_f	$\rho_w g\|z\|$
Displacement	u, v, w	0 [m]
Strain	ε_{ij}	0

The model was run for 50 years with 90 pumping wells placed in uniform spacing. It was found that the time variability of the pumping did not affect the results, and the wells were set to extract at a constant 8000 barrels per day (14.7 kg/s).

Note some of the parameters, initial and boundary conditions were updated with future versions of Jha *et al.*'s project. Due to this, there are some inconsistencies in the parameters depending on the iteration. The values stated here are derived from a combindation of the final thesis copy [8], AGU paper [9] and poster [10],

2.7.2 Model Results

Jha *et al.* was able to compare the field results to his model. By using the pumping and air injection method, the average water table dropped by 180 m, which is less than the 250 m observed in the field. Additionally, the subsidence was only 0.35 m, which is smaller than the expected value of at least 2 m. Jha *et al.* concluded that this indicates a possible misrepresentation of the elastic modulus of the subsurface. The other results were specific to the chosen fault plane and the AMF and UAF will be described separately.

2.7.2.1 AMF Fault

Jha *et al.* observed that the ΔCFF became negative (stabilized) around the area of the proposed hypocenter of the earthquake. Both down-dip shear traction and normal compression was promoted on the fault, which lead to a decline in ΔCFF. Down below, the normal stress changes to promoting un-clamping, but its not enough to overcome the stability promoted by the down-dip shear and the ΔCFF remains negative. As a result, according to Jha *et al.*'s model, the AMF fault becomes more stabilized everywhere due to groundwater extraction. This conclusion is counter to the results found by González *et al.* and suggests that further investigation is needed into the affects of groundwater extraction on fault stability.

2.7.2.2 UAF Fault

For this version, the antithetic fault was contained in the low permeability region. The results of the model suggested that ΔCFF becomes positive at a hypocenter around 3km in depth. The magnitude of ΔCFF is approximately 50 kPa [10]. This suggests the possibility that the antithetic fault had more favorable conditions for slip compared to the AMF. This will further be explored in this project.

Chapter 3

Theory and Methods Overview

3.1 COMSOL Modeling

COMSOL 5.3 was used for the poroelastic modeling portion of the project. The program is a Finite Element Method (FEM) code which has many user friendly interfaces. This section will describe the general steps used in COMSOL to build the model. At the end of the model, the pressure and stress changes were exported from COMSOL and read into MATLAB, where the stress rotations were calculated and plotted. The poroelastic and elastic models will be described separately. Additionally, both models were created in both 2D and 3D.

A detailed description of the workflow can be found online in the COMSOL documentation. The general process will be outlined here, but this description is not intended to be a thorough description of the workflow. The reader is referred to the Application Library Manual on-line documentation for completeness [19] [20].

3.1.1 Poroelastic Model Interface

For the poroelastic model, two different physics interfaces were used (*Fluid Flow* > *Porous Media and Subsurface Flow* > ***Darcy's Law*** and *Structural Mechanics* > ***Solid Mechanics***). The primary study was 3D and *Time Dependent.* The COMSOL interface could be easily navigated from a series of drop down menus (Figure 3-1).

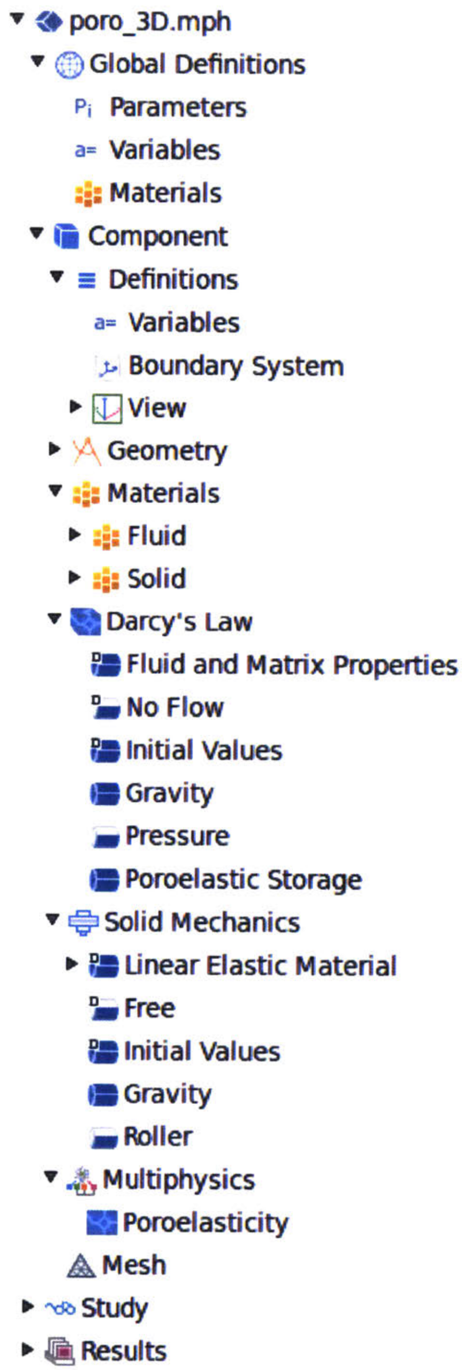

Figure 3-1: COMSOL Workflow Example for a Poroelastic Project

Once the file was created, the *Parameters* and *Variables* option was added to the *Global Definitions* section. The global parameters and variables will be described further for each project in Chapter 4 and Chapter 5.

Most of the work was completed in the *Component* drop down menu. The *Com-*

ponent > *Definitions* > *Variables* section was used to describe the domain-specific variables in the model. In contrast to the *Global Definitions* section, this could be used to define properties that were not constant across all domains in the model.

Next, the *Component* > *Geometry* was edited. The most notable complication of this section is the change in coordinate system between 2D and 3D. In 2D, the coordinate system is set to be x in the horizontal direction and y in the vertical direction. In 3D, the coordinate system is set to be x,y in the horizontal direction and z in the vertical direction. For this project, z will always be defined as the vertical axis and the outputted results were updated accordingly.

The *Component* > *Materials* section was then edited to include two blank materials, one for the fluid and one for the solid. Within thc fluid material section, the density and dynamic viscosity of the fluid were defined. For the porous media, the porosity, Poisson's ratio, density, permeability and Young's modulus were defined.

Next, the *Component* > *Darcy's Law* section was modified. This section adds the flow in porous media constraints. The original features included in the interface were *Fluid and Matrix Properties*, *No Flow* and *Initial Values*. The sections added were the *Poroelastic Storage Model*, *Gravity*, and *Pressure*. The specific boundary and initial conditions for the fluid flow will be described in Chapter 4 and Chapter 5.

The *Component* > *Solid Mechanics* section was modified and gave constrains on the porous media. The problem was set to be Quasi-Static. The original features were *Linear Elastic Material*, *Free* and *Initial Values*. The sections added were *Roller*, *Gravity*, *Boundary Load*, *Linear Elastic Material* > *Initial Stress and Strain* and *Linear Elastic Material* > *External Stress*. The initial stresses were added to ensure that there was no initial strain or deformation in the solid material caused by the gravity feature. The external stresses included the fluid pore pressure affecting the matrix. The specific boundary and initial conditions for the poroelastic solid will be described in Chapter 4 and Chapter 5.

A new addition to COMSOL 5.3, which was not present in the previous versions, is the *Component* > *Multiphysics* section. The *Poroelasticity* section creates a coupled interface between the *Solid Mechanics* and *Darcy's Law* physics nodes.

The meshing of the model is completed in the *Component* > *Mesh* section. COMSOL has a user friendly interface where different element sizes can be chosen for specified areas. There are 9 available element size options, ranging from Extremely Coarse (9) to Extremely Fine (1). Since the execution time was strongly dependent on the mesh, the element size varied for the 2D and 3D case. For the 2D case, the entire model was set to an Extremely Fine mesh size. For the 3D case, there were certain defined domains and boundaries that were set to have a finer mesh size. The geometry was also built to have a small buffer surrounding the fault zones for a finer mesh. The aquifer area, with the time dependent boundary conditions, was also set to have a finer mesh.

The time dependent study was computed in *Study* > *Step 1: Time dependent.* The fully-coupled solver was activated in *Study* > *Show Default Solver*, *Solver Configurations* > *Solution Time-Dependent Solver* > *Fully Coupled.* This is an important step for the 3D model, and is not explicitly stated in the on-line documentation.

The above workflow, on its own, describes the initialization of a poroelastic model. If all of the above mentioned features are properly inputted, a poroelastic model will be created with no displacement or strain for all times. Every model created began in this stage to ensure it was correctly initialized. Depending on the objectives of the projects, different features were then added to the *Darcy's Law* and *Solid Mechanics* interfaces. For example, a hydraulic head change was added to the Lorca project and contrastingly a producing well was added to the Wheeler Ridge project. These additions will be described in Chapter 4 and 5.

The results were then plotted in COMSOL or exported to MATLAB. The equations used by COMSOL will now be described. First, the governing equations for poroelasticity will be discussed. Next, it will be shown that these governing equations can be implemented using foundational Darcy's Law and Solid Mechanics equations.

3.1.2 Poroelastic Equations

3.1.2.1 Constitutive Relations for Poroelasticity

Within the theory of poroelasticity, there are two primary constitutive relationships [21]. The first equation provides a coupling for total stress ($\boldsymbol{\sigma}$), total strain ($\boldsymbol{\varepsilon}$) and pore pressure (p_f), with the elasticity matrix ($\mathbf{C}$) measured under drained conditions. The Biot-Willis coefficient (α) is the same constant described in Chapter 1.

$$\boxed{\boldsymbol{\sigma} = \mathbf{C}\boldsymbol{\varepsilon} - \alpha p_f \mathbf{I}} \tag{3.1}$$

The coupling term α does not depend on the properties of the fluid, but only on the elastic modulus of the drained porous media (K_d) and elastic modulus of the pure solid (K_s). The constant α can vary, but it is assumed to be 1 for the entirety of the project which is common for a soft soil.

$$\alpha = 1 - \frac{K_d}{K_s} \quad K_d \ll K_s \quad \alpha \approx 1 \tag{3.2}$$

The second constitutive equation relates the increment in fluid content (ζ) to volumetric strain (ε_{vol}) and fluid pore pressure. The volumetric strain can be thought of as the dilation of the porous matrix (positive is inflation and negative is deflation).

$$\boxed{p_f = \frac{1}{S}(\zeta - \alpha\varepsilon_{vol})} \tag{3.3}$$

The storage model can be defined using α, the compressibility of the fluid (χ_f) and porosity (θ). A high storage coefficient implies that there is a large volume of water that can be stored within the pores. With α=1, the equation can be simplified.

$$S = \theta\chi_f + (\alpha - \theta)\frac{1-\alpha}{K_d} \approx \theta\chi_f \tag{3.4}$$

Both of these equations can be derived using Darcy's Law and Solid Mechanics properties. The background for the equations will be described, and then the final equations applied in COMSOL will be stated.

3.1.2.2 Porous Matrix Governing Equations

Navier's equation is used for the modeling of the poroelastic material. A static equilibrium is assumed. The changes in the solid are assumed to equilibrate quickly, and the time dependence is assumed to only arise from the fluid equations. The constitutive equation is based on the total stress tensor ($\boldsymbol{\sigma}$), the gravity vector ($\mathbf{g}$) and the densities (average (ρ_{av}), fluid (ρ_f), drained matrix (ρ_d) and solid (ρ_s)).

$$- \nabla \cdot \boldsymbol{\sigma} = \rho_{av}\mathbf{g} = (\rho_f \theta + \rho_d)\mathbf{g} = (\rho_f \theta + (1 - \theta)\rho_s)\mathbf{g} \tag{3.5}$$

An important implication of Equation 3.5 is that the densities and porosity are assumed to be constants. If there are any density or porosity changes in the problem, the user must update them specifically.

Then, the solid is assumed to be a linear elastic material (total stress ($\boldsymbol{\sigma}$), total strain ($\boldsymbol{\varepsilon}$), pore pressure (p_f) and elasticity matrix ($\mathbf{C}$) measured under drained conditions). COMSOL initializes the model by adding terms to the linear elastic equation for the solid. In Equation 3.6, the $\boldsymbol{\sigma_0}, \boldsymbol{\varepsilon_0}$ are the initial stresses and strains, and the $\boldsymbol{\sigma_{ext}}$ is the added external stress for the pore pressure.

$$\boldsymbol{\sigma} - (\boldsymbol{\sigma_0} + \boldsymbol{\sigma_{ext}}) = \mathbf{C}(\boldsymbol{\varepsilon} - \boldsymbol{\varepsilon_0}) \tag{3.6}$$

The coupling term can then be added directly to the equation. For simplicity, the initialization terms will not be displayed again. It can be seen in Equation 3.7 that the shear portion of the stress tensor is independent of the pore pressure coupling. The non-deviatoric (or volumetric) part of the stress tensor is dependent on both strain and pore pressure.

$$\boldsymbol{\sigma} = \mathbf{C}\boldsymbol{\varepsilon} - \alpha p_f \mathbf{I} \tag{3.7}$$

In 2D, the plane strain assumption can be made and an example matrix is displayed here [20]. Recall that x is a horizontal direction and z is the vertical direction. Note that Equation 3.8 is equivalent to Equation 3.7.

$$\begin{bmatrix} \sigma_{xx} \\ \sigma_{zz} \\ \sigma_{xz} \end{bmatrix} = \frac{E}{(1+\nu)(1-2\nu)} \begin{bmatrix} 1-\nu & \nu & 0 \\ \nu & 1-\nu & 0 \\ 0 & 0 & 1-2\nu \end{bmatrix} \begin{bmatrix} \varepsilon_{xx} \\ \varepsilon_{zz} \\ \varepsilon_{xz} \end{bmatrix} - \alpha \begin{bmatrix} p_f \\ p_f \\ 0 \end{bmatrix} \tag{3.8}$$

.

For small deformations within the plane strain approximation, the strain can be related to the deformation, where u is in the x direction and w is in the z direction.

$$\varepsilon_{xx} = \frac{\delta u}{\delta x} \quad \varepsilon_{zz} = \frac{\delta w}{\delta z} \quad \varepsilon_{xz} = \frac{1}{2}\left(\frac{\delta u}{\delta z} + \frac{\delta w}{\delta x}\right) \quad \varepsilon_{xz} = \varepsilon_{zx} \quad \varepsilon_{xy} = \varepsilon_{zy} = \varepsilon_{yz} = 0 \tag{3.9}$$

3.1.2.3 Fluid Flow Governing Equations

Equation 3.3 can be derived using the Darcy's Law theory. The equation for the Darcy's Law interface is based on three primary equations [21]. First, the mass conservation equation is used and is dictated by the porosity (θ), fluid density (ρ_f), Darcy flow ($\mathbf{u}$), and a mass source term (Q_m). From this, the amount of fluid in the area is determined by the relative inflow and outflow, plus the fluid created or destroyed by the mass source term.

$$\frac{\delta}{\delta t}(\theta\rho_f) + \nabla \cdot (\rho_f \mathbf{u}) = Q_m \tag{3.10}$$

The left hand term of Equation 3.10 can be written to include the storage model (S) and pore pressure (p_f).

$$\frac{\delta}{\delta t}(\theta\rho_f) = \rho_f S \frac{\delta p_f}{\delta t} \tag{3.11}$$

Note that the implementation of Equation 3.11 changes the dependence of the equation from density and porosity to pressure. Pressure becomes the primary time dependent variable. Darcy's Law for flow can then be substituted into Equation 3.10.

$$\mathbf{u} = -\frac{\kappa}{\mu_f}(\nabla p_f - \rho_f \mathbf{g} \nabla D) \tag{3.12}$$

The mass source term (Q_m) can then be described. It is dictated by the change of volumetric strain of the porous matrix ($\frac{\delta}{\delta t}\varepsilon_{vol}$). The source term can be thought of as the expansion of the pore space [21]. As the pore space increases, the volume fraction available for the fluid also increase, and it allows for a liquid sink.

$$Q_m = -\rho_f \alpha \frac{\delta}{\delta t}\varepsilon_{vol} \tag{3.13}$$

Finally, Equations 3.11, 3.12 and 3.13 can be substituted into Equation 3.10. This final equation is the form used by COMSOL in the solver. In this formulation, the pressure (p_f) variable is solved for.

$$S\frac{\delta p_f}{\delta t} + \nabla \cdot [-\frac{\kappa}{\mu_f}(\nabla p_f - \rho_f \mathbf{g} \nabla D)] = -\alpha \frac{\delta \varepsilon_{vol}}{\delta t} \tag{3.14}$$

Equation 3.14 could alternatively be described using hydraulic head (H). H is the sum of pressure head H_P and elevation D, with elevation positive upwards.

$$H = H_P + D \quad H_P = \frac{p_f}{\rho_f \mathbf{g}} \tag{3.15}$$

3.1.2.4 Generalized Poroelastic Equations Applied in COMSOL

In summary, the final coupled equations that should be considered are as follows.

$$\boxed{-\nabla \cdot (\mathbf{C}\boldsymbol{\varepsilon} - \alpha p_f \mathbf{I}) = (\rho_f \theta + (1-\theta)\rho_s)\mathbf{g} \quad \varepsilon_{ij} = \frac{1}{2}\Big(\frac{\delta u_i}{\delta x_j} + \frac{\delta u_j}{\delta x_i}\Big)} \tag{3.16}$$

$$\boxed{S\frac{\delta p_f}{\delta t} + \nabla \cdot [-\frac{\kappa}{\mu_f}(\nabla p_f - \rho_f \mathbf{g} \nabla D)] = -\alpha \frac{\delta \varepsilon_{vol}}{\delta t}} \tag{3.17}$$

The fluid pressure (p_f) and displacements (u, w, v) are solved for by COMSOL. The resulting total stress tensor can then be calculated and outputted.

3.1.3 Elastic Model Summary

The elastic model was generated to be able to compare the magnitude of the stress changes and the differences in the stress patterns produced by the poroelastic and elastic models.

The elastic model does not take into account the fluid to solid coupling, so the Darcy Flow portion of COMSOL can be ignored. The porous solid was assumed to be a linear elastic media, and the standard equations are used.

$$-\nabla \cdot \boldsymbol{\sigma} = \rho_{av}\mathbf{g} \quad \boldsymbol{\sigma} = \mathbf{C}\boldsymbol{\varepsilon} \quad \varepsilon_{ij} = \frac{1}{2}\Big(\frac{\delta u_i}{\delta x_j} + \frac{\delta u_j}{\delta x_i}\Big) \tag{3.18}$$

As before, the model was initialized to include no initial deformation or strain. The specific applied loads will be discussed in Chapter 4. The displacements (u, w, v) were solved for by COMSOL and the resulting stress tensor was then outputted.

3.2 MATLAB Stress Calculations

3.2.1 Total Stress Tensor

The stress and fluid pressure values at the beginning and end times were exported from COMSOL and read into MATLAB ($\Delta\sigma_{xx}, \Delta\sigma_{yy}, \Delta\sigma_{zz}, \Delta\sigma_{xy}, \Delta\sigma_{xz}, \Delta\sigma_{yz}$ and Δp_f). The objective was to determine the normal (σ_n) and tangent (τ) along a curving fault plane, in the direction of the determined rake, using the Aki-Richards Convention. There are various ways to find the normal and tangent stresses, but the coordinate system transformation technique was applied. Three separate rotations were applied to the original tensor.

The original, unprimed, coordinate system is defined by the x, y, z Cartesian coordinates set up in COMSOL. A depiction of the curving fault in the original coordinate system is seen in Figure 3-2. First, the stress tensor was rotated into the primed coordinate system, which was defined with the x$'$ axis aligned with the strike of the fault. Next, the system was rotated to be aligned with the dip of the fault. Finally, it was rotated to be aligned with the rake of the fault.

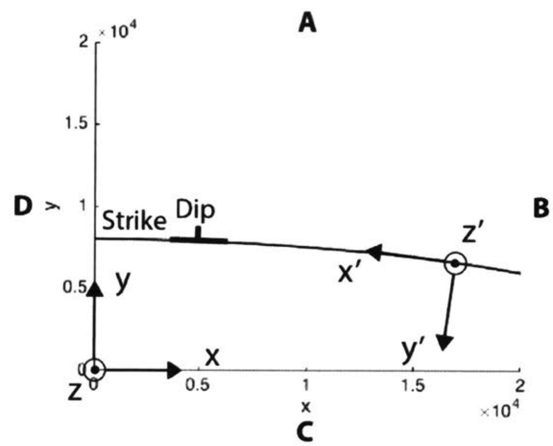

Figure 3-2: MATLAB Primed and Unprimed Coordinate Systems

The stress tensor was rotated from the unprimed coordinate system using the standard rotation matrix. Care was taken to notice if the rotation was in a clockwise or counter-clockwise rotation. In Figure 3-2, the displayed fault is dipping to $\approx$ **A**, with the strike of the fault approximately toward $\approx$ **D**. Since x' is aligned to the strike of the fault, the rotation angle phi is slightly less than π in a counter-clockwise rotation. The angle ϕ was determined by calculating the angle between x and $x^{'}$. x was defined as a unit vector.

$$x = [1, 0, 0] \tag{3.19}$$

Next, $x^{'}$ was determined. This varied depending on the set up of the problem. The most complicated set up was for a curving fault, and this example will be described here (Figure 3-3). The fault was assumed to have an elliptical trace. Then, $x^{'}$ could be found by determining the tangent to the ellipse, in the direction of the strike. Again, note that if the dip of the fault was in the opposite direction, the primed coordinate system would be flipped to align $x^{'}$ with the appropriate strike of the fault. An ellipse can described by a standard $y = f(x)$ equation.

$$\frac{x^2}{r_x^2} + \frac{y^2}{r_y^2} = 1 \qquad y = r_y^2 \sqrt{1 - \frac{x^2}{r_x^2}} \tag{3.20}$$

The derivative was then taken to determine the tangent to the ellipse.

$$\frac{\delta y}{\delta x} = -\frac{r_y x}{r_x^2}\left(1-\frac{x^2}{r_x^2}\right)^{-\frac{1}{2}} = -\frac{r_y x}{r_x^2}\left(\frac{y^2}{r_y^2}\right)^{\frac{-1}{2}} = -\frac{x\ r_y^2}{r_x^2\ y} \tag{3.21}$$

Recall that the tangent vector can be described in vector notation using the derivative of the equation.

$$\boldsymbol{t} = \left[1, \frac{\delta y}{\delta x}, 0\right] = \left[1, -\frac{x\ r_y^2}{r_x^2\ y}, 0\right] = \left[\frac{-y}{r_y^2}, \frac{x}{r_x^2}, 0\right] \tag{3.22}$$

Notice that the plus and minus signs have been chosen to align with the strike. The tangent vector can then be normalized.

$$\hat{\boldsymbol{t}} = \frac{\boldsymbol{t}}{\sqrt{\boldsymbol{t}\cdot\boldsymbol{t}}} = \frac{\boldsymbol{t}}{N} \qquad N = \sqrt{\frac{x^2}{r_x^4} + \frac{y^2}{r_y^4}} \tag{3.23}$$

Finally, the tangent vector pointing toward the strike can be found.

$$x' = \hat{\boldsymbol{t}} = \left[\frac{-y}{r_y^2 N}; \frac{x}{r_x^2 N}; 0\right] \tag{3.24}$$

The next coordinate system rotation was from the x', y', z' to the x'', y'', z'' system. The double primed coordinate system is set with the z'' axis aligned to the normal of the fault. This results in both the y'' and x'' axes on the plane of the fault. In this rotation, the x' coordinate system remained constant, and the y' and z' vectors are rotated by the dip (δ) (Figure 3-4).

Finally, the x'', y'', z'' is rotated to the x''', y''', z''' system. The tripled primed coordinate system is defined with the x''' axis aligned to the rake of the fault. The z'' axis is kept to be constant and the x'' and y'' axis are rotated by the rake (ψ) (Figure 3-5). Thus, there are three separate rotation matrices to be considered.

$$R_1 = \begin{bmatrix} cos(\phi) & sin(\phi) & 0 \\ -sin(\phi) & cos(\phi) & 0 \\ 0 & 0 & 1 \end{bmatrix} \quad R_2 = \begin{bmatrix} 1 & 0 & 0 \\ 0 & cos(\delta) & sin(\delta \\ 0 & -sin(\delta) & cos(\delta) \end{bmatrix} \quad R_3 = \begin{bmatrix} cos(\psi) & sin(\psi) & 0 \\ -sin(\psi) & cos(\psi) & 0 \\ 0 & 0 & 1 \end{bmatrix} \tag{3.25}$$

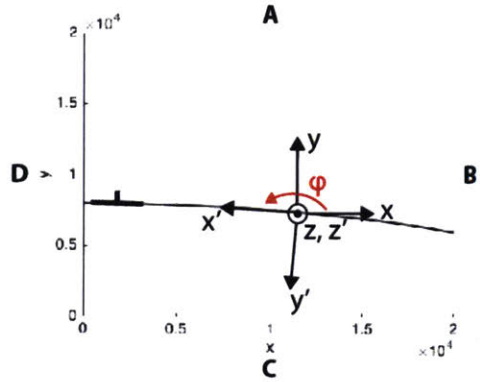

Figure 3-3: MATLAB Rotation to Align with Strike

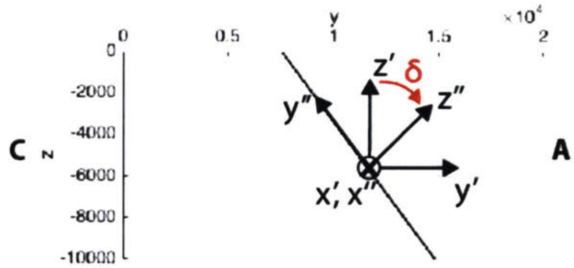

Figure 3-4: MATLAB Rotation to Align with Dip

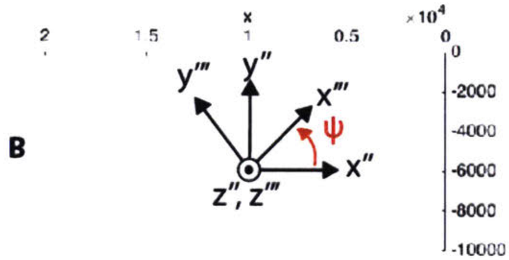

Figure 3-5: MATLAB Rotation to Align with Rake

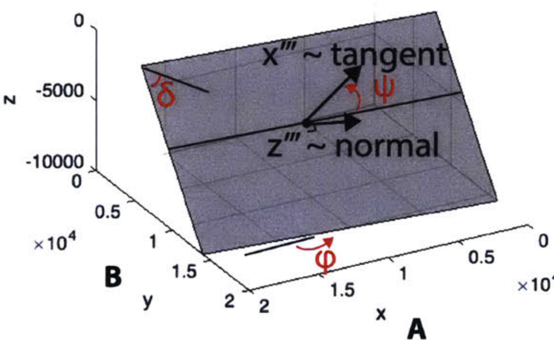

Figure 3-6: Final AMF Fault Normal and Tangent Stress Directions

The final coordinate system is then aligned with the $x^{'''}$ in the direction of the tangent stress, and the $z^{'''}$ vector is aligned with the normal of the fault. The final rotation matrix can be found by multiplying all of the constituent matrices.

$$R = R_3 R_2 R_1 =$$

$$\begin{bmatrix} cos(\phi)cos(\psi) - cos(\delta)sin(\phi)sin(\psi) & cos(\phi)sin(\psi) + cos(\delta)cos(\psi)sin(\phi) & sin(\delta)sin(\phi) \\ -cos(\psi)sin(\phi) - cos(\delta)cos(\phi)sin(\psi) & cos(\delta)cos(\phi)cos(\psi) - sin(\phi)sin(\psi) & cos(\phi)sin(\delta) \\ sin(\delta)sin(\psi) & -cos(\psi)sin(\delta) & cos(\delta) \end{bmatrix} \tag{3.26}$$

The final stress matrix can be determined using a standard rotation equation using the rotation matrix $\mathbf{R}$ and the associated transpose ($\mathbf{R^T}$).

$$\Delta\sigma''' = \mathbf{R}\Delta\sigma\mathbf{R^T} \tag{3.27}$$

As explained above, the $\Delta\sigma_{xz}^{'''}$ is the the tangent stress change and $\Delta\sigma_{zz}^{'''}$ is the normal stress change. Although both $\Delta\tau$ and $\Delta\sigma_n$ are functions of ϕ, δ, ψ, the full equations will not be provided here and the reader is referred to Equations 3.26 and 3.27 for the full expansion. Instead, $\Delta\tau$ and $\Delta\sigma_n$ will be provided as function of δ, ψ and ϕ is set to 0. This implies that the coordinate system is already aligned to the strike of the fault.

$$\Delta\sigma_{zz}^{'''}(\phi = 0, \delta, \psi) = \Delta\sigma_n = \Delta\sigma_{yy}sin(\delta)^2 + \Delta\sigma_{zz}cos(\delta)^2 - 2\Delta\sigma_{yz}cos(\delta)sin(\delta) \tag{3.28}$$

$$\Delta\sigma_{xz}^{'''}(\phi = 0, \delta, \psi) = \Delta\tau =$$
$$cos(\psi)(\Delta\sigma_{xz}cos(\delta) - \Delta\sigma_{xy}sin(\delta)) - sin(\psi)(\Delta\sigma_{yz}cos(2\delta) - \frac{1}{2}sin(2\delta)(\Delta\sigma_{yy} - \Delta\sigma_{zz})) \tag{3.29}$$

Note that these equations are the same as were derived by Jha *et al.* [8]. However, Equations 3.26 and 3.27 are more versatile and can be applied to numerous types of faults.

3.2.2 Effective Stress and Coulomb Failure Function

The effective stress ($\sigma_n^{'}$) was then calculated on MATLAB. The theory of effective stress is defined in Chapter 1. The stress convention is defined as negative for compression and positive for expansion. This dictates the signs of the equation.

$$\Delta\sigma_n^{'} = \Delta\sigma_n + \Delta p_f \tag{3.30}$$

Finally, the stability equation can be defined. The failure of a plane is determined by the relative balance between the shear and the normal force. A fault is assumed to fail when the shear stress is greater than the normal force times the coefficient of friction ($|\tau| > \mu|\sigma_n^{'}|$). The Coulomb Failure Function (ΔCFF) will be used to analyze fault stability, where μ is the coefficient of friction of the fault.

$$\Delta\text{CFF} = \Delta\tau + \mu\Delta\sigma_n^{'} = \Delta\tau + \mu(\Delta\sigma_n + \Delta p_f) \tag{3.31}$$

$\Delta\tau$ is the change in the shear force, and is defined as positive when slip in the direction of the predetermined rake is promoted. The normal stress change $\Delta\sigma_n$ is defined as positive if the fault is unclamped. Additionally, the p_f is positive when the pore fluid pressure increases. If any of these components increase, then the fault tends toward failure. In contrast, by definition, a negative (ΔCFF) means that the fault was stabilized by the stress change. A positive (ΔCFF) indicates that the fault is destabilized by the stress change, and that the system is closer to failure.

Note that in this theory, the coefficient of cohesive strength of the material has been set to 0 Pa for a plane (pre-existing fault). It is assumed that the strength of the surrounding rock is large enough that the fault will always fail before the rock.

3.3 Coulomb 3.4 Modeling

Coulomb 3.4 was an additional program that was used to verify the results of COMSOL. The program is fully executed through MATLAB. The program is thoroughly documented in an on-line USGS User Guide [3].

Coulomb 3.4 was intended to be a simplified version of the fluid to solid coupling aspect of poroelasticity. As the water is extracted from the aquifer, the aquifer contracts. In a simplified approximation, the aquifer will be modeled as a series of deflating point source in Coulomb 3.4. No other fluid flow is considered.

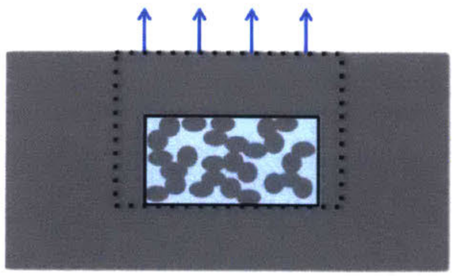

Figure 3-7: Fluid Extraction with Contracting Aquifer

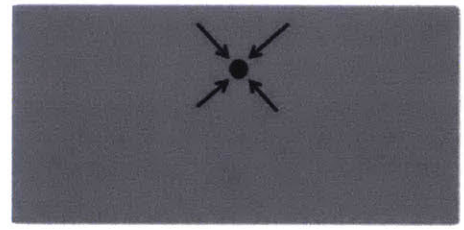

Figure 3-8: Contracting Point Source

As a brief overview of the program, Coulomb 3.4 uses the theory of source faults and receiver faults. Source faults have displacement and impact stress, receivers only receive stress and do not have slip. For the application in this project, the deflating aquifer was modeled as the 'source fault'. The program calculated the displacements, strains and stresses caused by the pore changes (inflation or deflation). This falls under the Kode 500 application [3]. Kode 500 describes a buried point source of expansion or contraction. The unit for inflation/deflation is the volume change associated with a spherical chamber (m^3), with expansion is defined as positive. The program used the theory from Okada to complete the calculations, and assumes an elastic half-space with uniform isotropic elastic properties. The Okada calculations are described in the original 1992 paper [22]. The internal deformation fields are determined for an isotropic expansion point, and analytic solutions are found. The internal strain and stress fields are then evaluated using the Lamé parameters in the standard equations.

$$\sigma_{ij} = \lambda \varepsilon_{kk} \delta_{ij} + 2\mu\varepsilon_{ij} \quad \varepsilon_{ij} = \frac{1}{2}\Big(\frac{\delta u_i}{\delta x_j} + \frac{\delta u_j}{\delta x_i}\Big) \tag{3.32}$$

The aquifer or reservoir was modeled as a series of deflating point sources. As mentioned before, the input into Coulomb 3.4 is the elastic solid volume change at a point source. In order to approximate the volume change of the solid per unit of fluid removed, the poroelastic nature of the subsurface must be considered. The solution developed by Ming Fang, MIT was used to find the relationship between pressure/hydraulic head decrease and volume change [23]. The solution for the deformation by pore pressure in a uniform poroelastic core was used.

For the solution, consider a uniform elastic sphere of radius a with a uniform pressure change in a smaller core of radius b ($b < a$). The sphere was assumed to have a constant porosity θ and was saturated with a fluid. There is a linear strain induced by the pressure change in the inner core. In addition to the linear strain, there is also a elastically deformed strain. They can be added to evaluate the total strain.

$$\varepsilon_P + \varepsilon_d = \beta \delta p \mathbf{I} \quad + \quad \frac{1}{2\mu}\sigma - \frac{\lambda}{2\mu(3\lambda + 2\mu)} tr(\sigma)\mathbf{I} \tag{3.33}$$

The pore expansion coefficient of compressibility β is assumed to be constant. From this relationship, the displacement (u) outside of the porous core can then be derived [23].

$$u = Br + C\frac{1}{r^2} \quad (b < r < a) \tag{3.34}$$

$$B = \frac{2\beta\delta p}{3(1-\nu)}\left(\frac{1-2\nu}{1-\nu}\right)\left(\frac{b}{a}\right)^3 \quad C = \frac{\beta\delta p}{3}\left(\frac{1+\nu}{1-\nu}\right)b^3 \tag{3.35}$$

Assuming that $a \gg b$, $\frac{b}{a} \to 0$, the B term approaches 0. Then, after setting $r = b$, the displacement (u) can be thought of as the change of radius of the inner core. Recall that the change in radius can be related to the change in volume.

$$\begin{aligned} V &= \frac{4}{3}\pi r^3 \\ \delta V &= 4\pi r^2 \delta r \\ \delta V(r = b) &= 4\pi b^2 u \end{aligned} \tag{3.36}$$

Next, the C term is substituted into the displacement solution, and $r = b$.

$$
\begin{aligned}
u &= C\frac{1}{r^2} \\
u &= \frac{\beta\delta p}{3}\Big(\frac{1+\nu}{1-\nu}\Big)\frac{b^3}{r^2} \\
u(r=b) &= \frac{\beta\delta p}{3}\Big(\frac{1+\nu}{1-\nu}\Big)b
\end{aligned}
\tag{3.37}
$$

The displacement (u) can be substituted into the change in volume.

$$
\begin{aligned}
\delta V &= 4\pi b^2 u \\
\delta V &= 4\pi b^2\frac{\beta p}{3}\Big(\frac{1+\nu}{1-\nu}\Big)b \\
\delta V &= \delta p \quad \frac{4\pi b^3}{3} \quad \beta\Big(\frac{1+\nu}{1-\nu}\Big)
\end{aligned}
\tag{3.38}
$$

This equation can separated into three terms. First, the change of pressure, which will be the dependent variable. The next term can be thought of as the volume of the original porous core, or the aquifer, which undergoes the change in pressure. In the model, this volume will be divided up into several sources in the shape of the aquifer. The last term is based on the elastic properties of the medium, and affects the resulting ratio of pressure change to volume change.

In Coulomb 3.4, this calculated volume change, Young's Modulus and Poisson ratio, was input into the program. The shear stress and normal stress changes and and ΔCFF were calculated for a specified strike, dip and rake. The Aki-Richards convention was used to describe the fault, as described in Chapter 1.

Chapter 4

Lorca, Spain

The objectives of the Lorca, Spain project were three-fold.

1. Validate the poroelastic COMSOL and MATLAB work flow by comparing it to the simplified Coulomb 3.4 Model (Section 4.2.2)

2. Present the poroelastic results and propose a hypothesis for the Lorca 2011 earthquake (Section 4.2.3)

3. Compare the results from the poroelastic model to an elastic model (Section 4.2.4)

The project set-up will first be described for COMSOL (elastic and poroelastic) and Coulomb 3.4. The results will then be presented for the elastic, poroelastic and Coulomb 3.4 models.

4.1 Problem Setup

The focus area of this project is shown in Figure 4-1. The AMF Fault, and Alto Guadalentín basin can be seen plainly from Google Earth, and this was used as a basis to set up the project.

In Figure 4-1, Lorca is shown by the red circle and the 2011 earthquake epicenter is shown by the yellow star. Recall that there is a large-scale NNW-SSE shortening

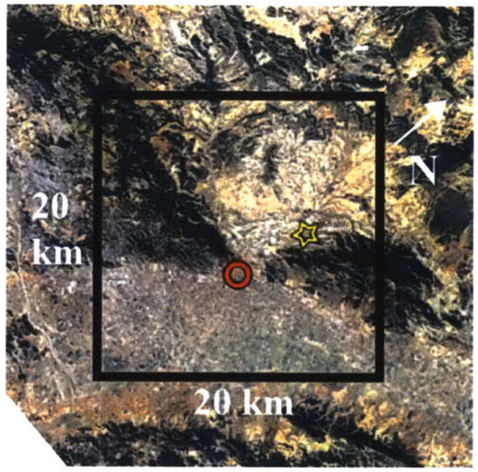

Figure 4-1: Lorca Focus Area from Google Earth

direction. The Alto Guadalentín Basin can clearly be seen as the flat area ~SE of the city. The AMF intersects with the city, and divides the basin region from the mountains. The 20 km x 20 km region indicated by the black box was the focus of the study.

4.1.1 COMSOL Input

4.1.1.1 Geometry

Since the Lorca, Spain section was also intended to duplicate the results of Jha *et al.* the models were closely paralleled. The basic parameters of the model were intially determined from a combination of Jha *et al.*'s poster [10], thesis [8] and AGU paper [9]. However, additional details were found in literature and considered.

The first step was to determine the general shape of the block, and the locations of the AMF, UAF and aquifer. The model was built as a 20km (x) x 20km (y) x 10km (z) region. The horizontal axis was set to be aligned with the strike of the AMF. The coordinate system was rotated -50° from North, resulting in the $x+$ axis toward ~NE, $y+$ axis toward ~NW and $z+$ axis pointed up. Based on the Google Earth image, it was found that the AMF could be modeled with an elliptical trace. In Figure 4-2, the trace of the AMF is shown in green, and the proposed UAF is shown in purple. The location of the AMF fault was chosen based on the surface expression. The UAF fault was chosen to be 8 km away from it, based on Jha *et al.*'s model [10]. Although the UAF is a blind thrust fault, Jha *et al.* approximated the location from the InSAR relocation study [15]. The Google Earth region (Figure 4-2) was replicated on MATLAB (Figure 4-3).

Figure 4-2: Lorca Domain on Google Earth

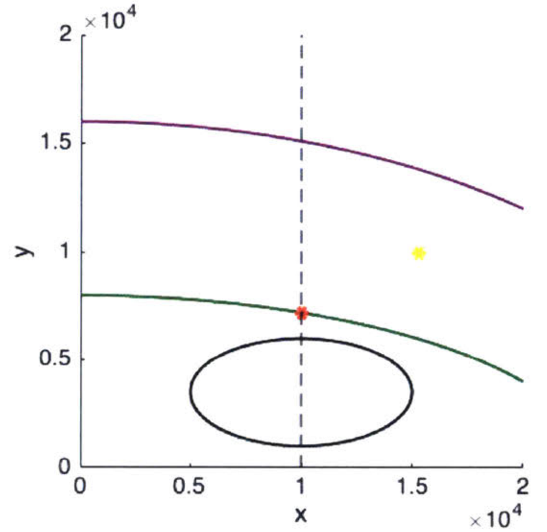

Figure 4-3: Lorca Domain on MATLAB

However, in contrast to Jha *et al.*, the UAF was not extended to the full 10 km depth of the model and instead terminated at the AMF. It was modeled in this way because it was assumed to be more geologically accurate for an antithetic fault.

The Alto Guadalentín Basin was set to extend laterally from the x axis to 250 m from the AMF (green), and to a depth of 1 km [4] [6]. Within the basin region, the permeability exponentially decreases with depth. The permeability of the basin was again chosen based on Jha *et al.*'s models. Out side of this region, it was assumed to be very low permeability [24]. From this point on, the actual area where water was being extracted will be referred to as the aquifer, and the high permeability rock of the Alto Guadalentín Basin will be referred to as the basin.

The aquifer was modeled to have an elliptical shape. It can be seen by the black ellipse in Figure 4-3. The location and shape of the aquifer was chosen based on the ground deformation trends shown by Gonzalez et al [6]. However, the aquifer was assumed to be symmetric.

Furthermore, the elliptical aquifer and elliptically curving faults were chosen to minimize sharp angles and thus reduce artificial stresses at boundaries. As shown in Equation 4.1, the elliptical faults and aquifer can be described by the center of the ellipse (c_x, c_y) and the two radii (r_x, r_y). These values, and the dips of the faults, are shown in Table 4.1. The dip values for the AMF and UAF in the literature were within a certain range (45°-70°), and the values for this project were chosen to match Jha *et al.* [8].

$$\frac{(x-c_x)^2}{r_x^2} + \frac{(y-c_y)^2}{r_y^2} = 1 \tag{4.1}$$

Table 4.1: Lorca Aquifer, AMF and UAF Geometry

	c_x (km)	c_y (km)	r_x (km)	r_y (km)	dip (°)
Aquifer	10	3.5	5	2.5	-
AMF	0	0	23.1	8	54 to $y+$
UAF	0	0	30.2	16	50 to $y-$

The final COMSOL model can be seen in Figure 4-4. The basin, aquifer, AMF and UAF are depicted relative to the $x+$,$y+$ and $z+$ locations.

4.1.1.2 Initial Conditions and Boundary Conditions

In COMSOL, the boundary and initial conditions were entered into the appropriate sections of *Darcy's Law* and *Solid Mechanics.* This section of the report is only intended to list the conditions specific to the Lorca project. Refer to Chapter 3 for a complete description of the work flow. As displayed in Table 4.2, the same initial conditions were used in this model as were used in Jha *et al.*'s research.

For the *Solid Mechanics* section, the initial stress state was controlled through the *Linear Elastic Material* > *Initial Stress* and The *Linear Elastic Material* > *External Stress* section. The *Initial Stress* included the σ_{ii} stresses listed in Table 4.2, and the *External Stress* included the pore pressure (p_f). For the boundary conditions, the *Free* condition was applied to the top surface ($z+$), while the *Roller* condition was

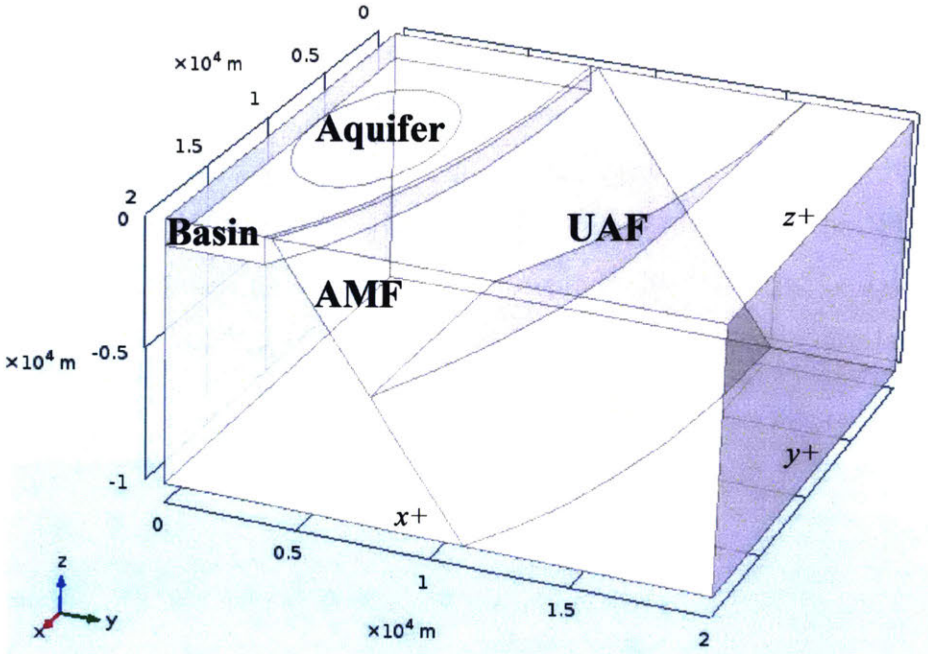

Figure 4-4: COMSOL 3D Lorca Geometry Image

Table 4.2: Lorca Initial Conditions

Stress in z direction	σ_{zz}	-$\rho_{av}g\|z\|$
Stress in x direction	σ_{xx}	-1.5$\rho_{av}g\|z\|$
Stress in y direction	σ_{yy}	-2$\rho_{av}g\|z\|$
Pore Pressure	p_f	$\rho_w g\|z\|$
Displacement	u, v, w	0 [m]
Strain	ε_{ij}	0

applied to all other sides (x+, x-, y+, y-, z-). Due to the way that COMSOL applies initial stresses, there was no additional normal compression needed on the y+ side. The initial condition of σ_{yy0} = -2$\rho_{av}g|z|$ was sufficient to replicate the thrust fault.

For the *Darcy's Law* boundary conditions, the *Pressure* condition was applied to the top surface (z+) and p_f was set to 0 Pa. The *No Flow* condition was applied to all other sides (x+, x-, y+, y-, z-). Note that all other reference pressures were also set to 0 Pa so there was no induced flow.

Finally, as introduced in Chapter 1, the poroelastic model must consider two time dependent conditions; both the flow effects (*Darcy's Law* > *Hydraulic Head*) and the unloading stresses (*Solid Mechanics* > *Boundary Load*). The boundary load is added to account for the density change in the porous system. COMSOL does not automatically adjust the mass as the water is being removed, so a boundary load must be added to represent the change from water to air in the aquifer. The updated COMSOL interface for the Lorca project is shown in Figure 4-5.

Figure 4-5: Lorca COMSOL Interface

Both the hydraulic head change and unloading boundary load are time and space dependent functions. Both of these effects are directly related to the water extraction pattern and they follow the same spacial trends. The distribution was calculated using the curve fitting toolbox on MATLAB. The distribution is shown in Figure

4-6 and the function is described in Equation 4.2 and Table 4.3. The pumping was modeled to be a function of x, y and was set to be the maximum (yellow) in the middle of the aquifer ellipse and tapering to 0 (blue) at the edges.

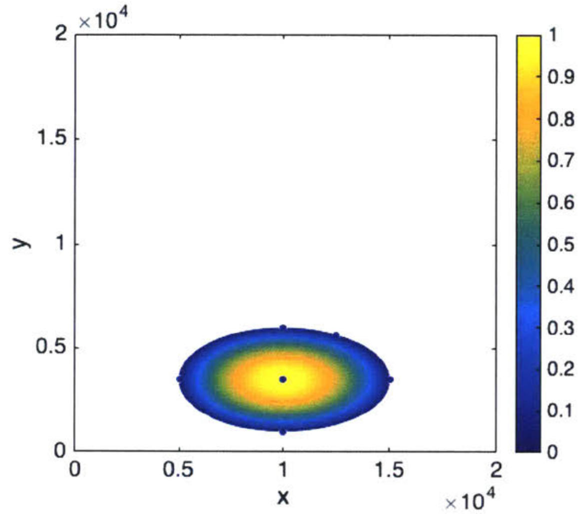

Figure 4-6: Spatial Distribution of Water Removal from Lorca Aquifer

$$fit_{3D}(x, y) = p_{00} + p_{10}x + p_{01}y + p_{20}x^2 + p_{11}xy + p_{02}y^2 \tag{4.2}$$

Table 4.3: Lorca Coefficients for Water Extraction 3D Fit

p_{00}	-4.96
p_{10}	0.0008 [m^{-1}]
p_{01}	0.00112 [m^{-1}]
p_{20}	-4e-08 [m^{-2}]
p_{11}	-1.828e-22 [m^{-2}]
p_{02}	-1.6e-07 [m^{-2}]

The final functions were determined by multiplying the hydraulic head change or the unloading stress by the 3D fit. The amount of hydraulic head change (δH) over 50 years is not known exactly, and it was approximated to be 5 [m/yr]t extracted at the center of the aquifer and tapering to 0 [m/yr]t at the edges [8] [6] [14].

The boundary load is a function of the hydraulic head change (δH), porosity (θ), water density (ρ_w) and gravity (g). Thus, the hydraulic head change can be described by Equation 4.3, and the unloading stress load can be described by Equation 4.4. Similar methods could be used to find the parabolic function in 2D, but the calculations are not shown here.

$$\boxed{\delta H_{3D} = fit_{3D} \times \delta H = fit_{3D} \times (-5[\mathrm{m/yr}]t)} \tag{4.3}$$

$$\boxed{Load_{3D} = fit_{3D} \times |\delta H \theta \rho_w g|} \tag{4.4}$$

4.1.1.3 Updated COMSOL Poroelastic Equations

After the addition of the hydraulic head and boundary load features, the final equations are modified within COMSOL. The boundary load force is represented by **F**.

$$-\bigtriangledown \cdot (\mathbf{C}\boldsymbol{\varepsilon} - \alpha p_f \mathbf{I}) = (\rho_f \theta + (1-\theta)\rho_s)\mathbf{g} + \mathbf{F} \quad \varepsilon_{ij} = \frac{1}{2}\Big(\frac{\delta u_i}{\delta x_j} + \frac{\delta u_j}{\delta x_i}\Big) \tag{4.5}$$

The Darcy flow equation does not have to be modified since the hydraulic head change could be directly fed into the pressure terms ($p_f = H\rho_f g$).

$$S\frac{\delta p_f}{\delta t} + \bigtriangledown \cdot [-\frac{\kappa}{\mu_f}(\bigtriangledown p_f - \rho_f \mathbf{g} \bigtriangledown D)] = -\alpha \frac{\delta \varepsilon_{vol}}{\delta t} \tag{4.6}$$

4.1.1.4 Parameters and Variables

The parameters and variables chosen for the poroelastic aspect of the project can be seen in Table 4.4. Note that the permeability is the only variable or parameter that does not apply to the entire region. The model was run for 50 years, replicating the initiation of pumping in the 1960s [14].

Table 4.4: Lorca General Parameters

Coefficient of Friction	μ	0.47
Poisson's Ratio	ν	0.25
Biot Coefficient	α	1
Porosity	θ	0.1
Compressibility of Water	c_w	4×10^{-10} [Pa^{-1}]
Viscosity of Water	μ_w	1 [cP]
Storage Coefficient	S	$\theta\ c_w$
Solid Density	ρ_s	2600 [kg/m^3]
Density of Water	ρ_w	1000 [kg/m^3]
Drained Density	ρ_d	$(1\text{-}\theta)\rho_s$
Average Density of Rock	ρ_{avg}	$\rho_d+\theta\rho_w$ [kg/m^3]
Young's Modulus	E	$E_m z + E_b$
	E_m	-7.99 [MPa/m]
	E_b	100 [MPa]
Permeability within Basin	k	$k_{max}e^{a_k z}$
	k_{max}	1000 [mD]
	a_k	$(7\log(10))/1000$ [m^{-1}]
Permeability outside of Basin	k	0.0001 [mD]

4.1.1.5 Elastic Model Specifications

Since there is no fluid flow component in the elastic model, only the boundary load is considered (Equation 4.4). This is the only time dependent aspect of the model. Note that the other boundary and initial conditions were appropriately modified for the elastic model since there was a no flow component. The elastic model was run and compared to the full poroelastic model and the results by González *et al.*

4.1.2 Coulomb 3.4 Input

The theory behind the Coulomb 3.4 modeling is described in Chapter 3. Recall that in Equation 3.38, there are three groups of terms that need to be considered when calculating the volume change of a solid induced by the pore pressure change: the pressure change, the original volume of the effected porous core and the elastic properties of the medium. For the approximation, the aquifer was subdivided, and each point source acted like a deflating porous core. The distribution is shown in Figure 4-7. The numbers are a numbering system for the point sources, from 1 to 38.

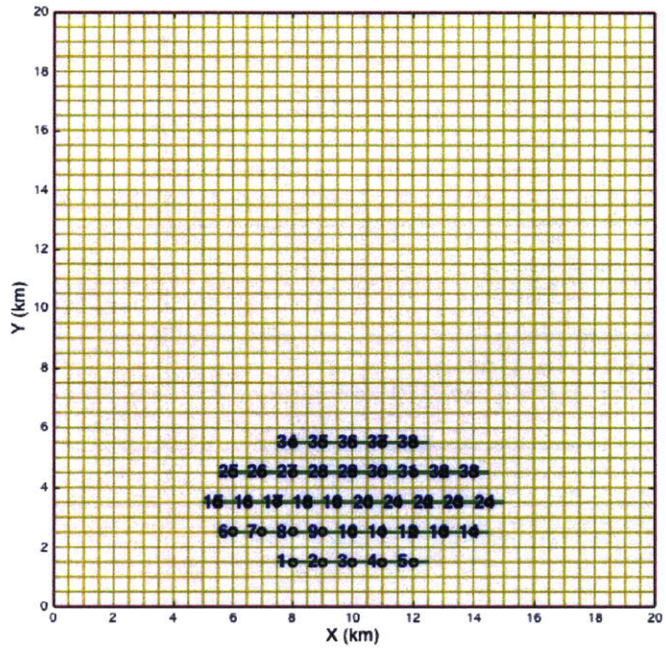

Figure 4-7: Coulomb 3.4 Lorca Setup

The original equation for the Coulomb 3.4 input, derived in Chapter 3, is shown.

$$\delta V = \delta p \quad \frac{4\pi b^3}{3} \quad \beta\left(\frac{1+\nu}{1-\nu}\right) \tag{4.7}$$

This equation was modified for each point source. The total fluid pressure change is 0 at the edges of the aquifer, and $250[\text{m}](\rho_w g)$ in the middle of the aquifer. The hydraulic head change function that was calculated in MATLAB (Equation 4.3) will be used to determine the pressure change for each point source.

$$\delta p = \rho_f g \delta H \tag{4.8}$$

The volume of the aquifer is equivalent to the area of the ellipse ($r_x r_y \pi$) times the depth (d) to which water was being extracted. This volume was then divided by the desired number of point sources (n_{ps}).

$$V_{aq} = r_x r_y \pi d \quad V_{aq_{ps}} = \frac{V_{aq}}{n_{ps}} \tag{4.9}$$

Recall that the coefficient of compressibility (β) can be described by the bulk modulus (K_b) and also Young's Modulus (E).

$$\beta = \frac{1}{K_b} = \frac{3(1-2\nu)}{E} \tag{4.10}$$

These steps update Equation 4.7 to a version that is suitable for the Lorca project. The constants for this equation can be found in Table 4.5

$$\delta V_{ps} = \rho_w g \delta H_{ps} \quad \frac{V_{aq}}{n_{ps}} \quad \frac{1}{E}\left(\frac{3(1-2\nu)(1+\nu)}{1-\nu}\right) \tag{4.11}$$

An image solution was applied to take into account the COMSOL Boundary conditions. An identical distribution of deflating point sources was applied in a reflection across the x axis. This was used to act like the *Roller* condition in COMSOL.

For a more accurate comparison of the COMSOL and Coulomb 3.4 solutions, a couple changes were made to the COMSOL model and a simplified 2D model was run. In this version, the permeable basin was set to be the same area of the aquifer, extended to a depth of 250 m. The Young's Modulus was set to a constant of 40 GPA. Additionally, the boundary load was turned off since this unloading effect would not be captured in the Coulomb 3.4 modeling. Lastly, the ΔCFF was calculated without the pore fluid pressure component, and this is referred to as the "Dry" ΔCFF.

Table 4.5: Coulomb 3.4 Lorca Input

Density of Water	ρ_w	1000 [kg/m^3]
Gravity	g	9.81 [m/s^2]
Hydraulic Head Change in Aquifer	δH_{ps}	$fit_{3D}(x,y)\times$ 250[m]
Total Volume of Aquifer	V_{aq}	9.8×10^9 [m^3]
Number of Point Sources	n_{ps}	38
Mean Young's Modulus of Entire Region	E_{av}	40 [GPa]
Coefficient of Friction	μ	0.47
Poisson's Ratio	ν	0.25

4.2 Results and Discussion

4.2.1 Problem Context

The primary objective of this project is to propose a hypothesis for the role that the extraction of the Alto Guadalentín Basin played in the May 11, 2011 Lorca Earthquake. It is proposed that the 2011 earthquake was tectonically driven, but that the extraction of the aquifer may have lead to zones of increased destabilization. This problem will first be analyzed from the perspective of the published literature, and the evidence for specific rupture planes will be explored. Next, the results from this FEM study will be analyzed and the hypothesis for the earthquake will be proposed.

The reader is referred to Chapter 2 for an overview of the primary papers used. As a summary, the rupture plane for the earthquake is currently unknown and there is evidence to support various source mechanisms. Unfortunatley, there was no surface rupture found to provide support for a specific plane [4], and the true rupture plane is a topic of debate. For this project, the two planes that will be investigated are the Alhama de Murcia (AMF) and an unidentified antithetic fault (UAF) which branches with an opposite dip from the main segment. Both of these solutions would be in agreement with the large-scale trends of the south-east Spain, where there is a NNW-SSE shortening direction [4]. Moving forward, both planes will be equally considered.

First, the location the epicenter plane will be considered. In the literature, Martínez-Díaz *et al.* and Pro *et al.* both conclude that the epicenter was located on a fault plane to the W-NW of the main trace of the AMF. However, there are different opinions on the actual fault plane that ruptured. Martínez-Díaz *et al.* suggest that the rupture plane was a fault that was parallel to the AMF but ~N of Lorca. Pro *et al.* conclude a similar scenario, and specifically name the Cejo de los Enamorados Fault (CEF) as the rupture plane. Although Martínez-Díaz *et al.* recognize the presence of the antithetic fault, it is not proposed as a possibility for the rupture plane. However, the UAF as the rupture plane would also agree with the locations of the epicenters ~W-NW of the AMF, and thus the UAF as the main rupture plane is also supported by this argument.

In addition to the location, the official strike and dip of the plane is still undetermined. Recall that there are two main solutions from the moment tenser inversions. The first solutions are from the Spanish Instituto Geografico Nacional (IGN), the Istituto Andaluz de Geofisica (IAG), the Global Centroid Moment Tensor solution (GCMT) and the University of Nice (Geoazur), and are consistent with a fault with a strike N245°E and dip 45° (AMF). Alternatively, the Italian Instituto Nazionale di Geofisica e Vulcanologia (INGV), the German Geo Forschungs Zentrum (GFZ) and the US Geological Survey (USGS) support a fault with a strike of N50°E and dip 50° (UAF). Thus, there is evidence to support the strike and dip of both the AMF and UAF from moment tensor inversions. The UAF cannot be ruled out from this argument. For this project, the location and dip direction of this planes were set as constants. Due to the high variability in the literature, the rake of the fault is the only parameter that was varied and the slip direction will now be explored.

Consistently, the rupture slip was found to have an approximate SW direction, toward the city of Lorca. Refer to Figure 4-1 for the relative location of Lorca and the epicenter. This direction of slip was identified from both the aftershock relocation and the directivity analysis [5]. Another interesting conclusion from the directivity analysis is the definite up-dip portion of the slip. This supports the proposed left lateral-reverse motion. From the definition of the rake, the SW and up-dip motion of the plate can be described by rake values between 0°-90°. Thus, the slip direction found in the field could be satisfied by both the UAF and AMF solution, as long as the rake is appropriately defined.

Finally, the InSAR evidence will be examined. It was found that both the AMF and UAF could be supported by the InSAR results. The true fault plane could not be discriminated for several reasons (provided in Chapter 2). However, it is the slip direction was much steeper in the InSAR results, and the rake was proposed to be 77°. This could be because InSAR data is more sensitive to the vertical component of the movement.

As a result, there is no field or published data found that could conclusively rule out the UAF as the rupture plane, and most of the evidence could support either the AMF or UAF. However, notably, some located positions of the epicenter are to the W-NW of the AMF. These locations increase support for the UAF solution. With the published literature in mind, the results of the FEM study will be considered.

4.2.2 Coulomb 3.4 and COMSOL Results Comparison

First, the Coulomb 3.4 results will be presented. Recall that the Coulomb 3.4 and modified COMSOL models were run to be able to better understand the poroelastic effect. It was proposed that if both sets of results matched, that the confidence in the COMSOL-MATLAB workflow would increase.

It can be seen in Figure 4-8 that there is a high level of agreement in distribution and magnitude of the stress changes. The figures depict the results from a cross section that bisects the aquifer (dashed line in Figure 4-3). The AMF within this cross section is depicted by the solid line in 4-8.

From the simplified model, it can be deduced that the shear and normal stress changes and ΔCFF have complex spatial distributions. Moving forward, it is important to consider that the stress change on the fault plane is highly dependent on the dip and location of the fault. If the location of the fault relative to the aquifer

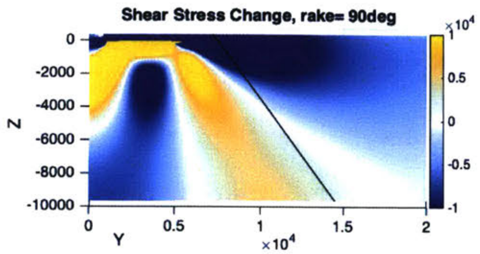

(a) COMSOL
Shear Stress Change [Pa]

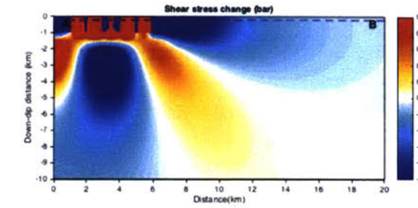

(b) Coulomb 3.4
Shear Stress Change [bar]

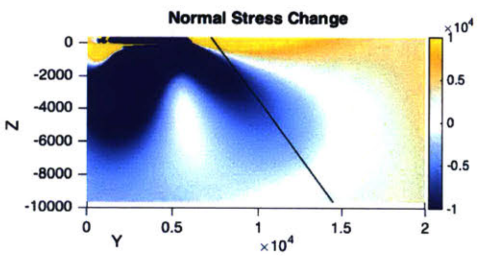

(c) COMSOL
Normal Stress Change [Pa]

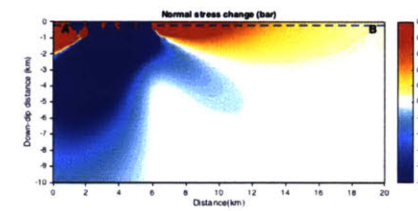

(d) Coulomb 3.4
Normal Stress Change [bar]

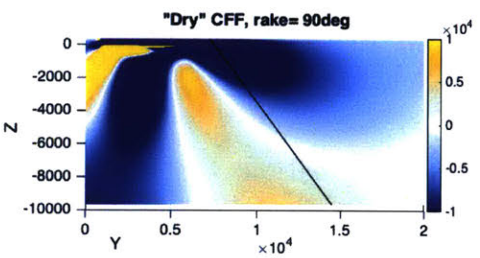

(e) COMSOL 'Dry' ΔCFF [Pa]

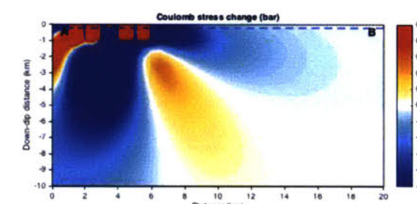

(f) Coulomb 3.4 ΔCFF [bar]

Figure 4-8: Comparison of COMSOL Poroelastic and Coulomb 3.4 Results

was different, then the fault plane could move from a state of stability to instability (Figure 4-8e). However, for the remainder of this analysis the location and dip is assumed to be known and the affect of the rake is the only factor that is investigated.

Using Coulomb 3.4 was an important step for verification for the COMSOL and MATLAB workflow, and indicated that the implemented methods were functioning properly. Once these plots appeared to be the same, there was an increased confidence in the outputted model. For example, before the parabolic fit was implemented in the hydraulic head decrease, there were unnatural stresses occurring at the transition from the high permeability aquifer to the low permeability adjacent rock. These increased stresses were large and misleading, and they were only identified as being incorrect when the COMSOL results were compared to the Coulomb 3.4 results.

The project then proceeded with the confidence that the poroelastic effect was correctly being replicated in COMSOL.

4.2.3 COMSOL Poroelastic Results and Hypothesis

4.2.3.1 Pore Pressure and Stress Changes

The poroelastic results can be seen in Figure 4-9 and 4-10. The images depict the stress changes along the fault plane, if each of the faults were viewed from the $y+$ direction, or NW. These plots were generated using the 3D feature in COMSOL. Depicted on the fault planes is the approximate location of the 2011 earthquake hypocenter (yellow) and the city of Lorca (red). Since the results are being collapsed onto a plane, the yellow star simply represents the depth of the earthquake and is set to 4.6 [km] [5]. Initially, the rake of the faults is set to 90°. This direction of slip can be easily understood, and is a good starting place for the evaluation. Eventually, the rake will be varied and the effects analyzed.

As shown in Figures 4-9a and 4-10a, the pore fluid change has a stabilizing affect on both the AMF and the UAF. This is an expected result since water is being removed from the subsurface, and a decrease in fluid pressure increases the stability of a fault. The pressure changes are naturally higher for the AMF, since that fault is closer to the aquifer.

The normal stress change is substantially different for the AMF (Figure 4-9b) and UAF (Figure 4-10b). It can be seen that, in general, the contraction of the aquifer causes a clamping on the AMF and an un-clamping on the UAF. The shear stress change also exhibits different trends for each fault. Recall that the rake of this

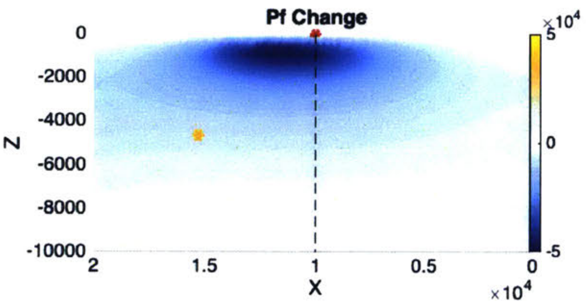

(a) AMF p_f Change [Pa]

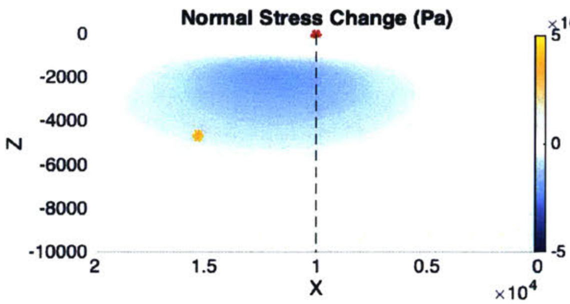

(b) AMF Normal Stress Change [Pa]

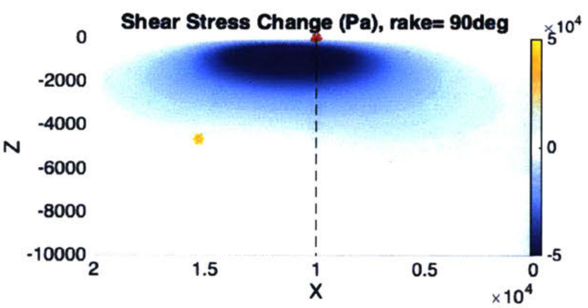

(c) AMF Shear Stress Change [Pa]

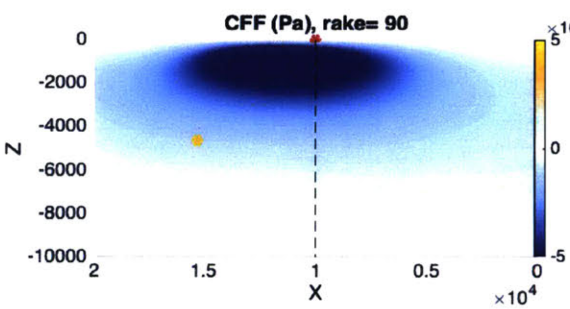

(d) AMF ΔCFF [Pa]

Figure 4-9: 3D Poroelastic Results for AMF with 90° Rake

example is set to be a reverse fault. The AMF (Figure 4-9c) is in general stabilized by the pumping of the aquifer but the UAF (Figure 4-10c) is stabilized in the top half and destabilized in the bottom half.

Combining these results, the ΔCFF is different for the AMF and UAF. The AMF (Figure 4-9d) is almost entirely stabilized by the contraction of the aquifer. The large pore pressure change on the AMF is a significant contributing factor. In contrast, the p_f does not play as much of a role on the UAF (Figure 4-10d), and is stabilized near the top and destabilized lower down. Note that in this particular fault location and dip, the destabilization of the UAF occurs adjacent to the hypocenter of the 2011 earthquake in x, y and z. This is an important result that will be further explored.

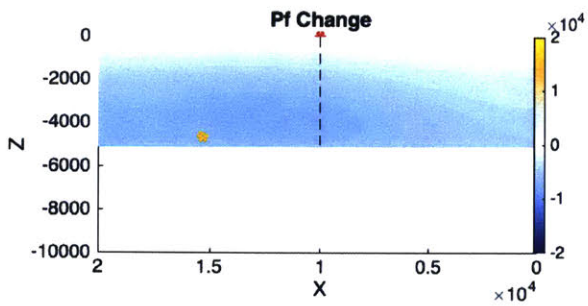

(a) UAF p_f Change [Pa]

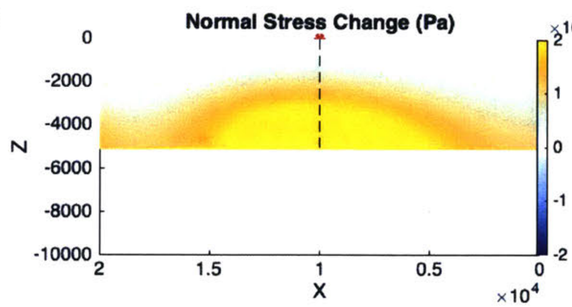

(b) UAF Normal Stress Change [Pa]

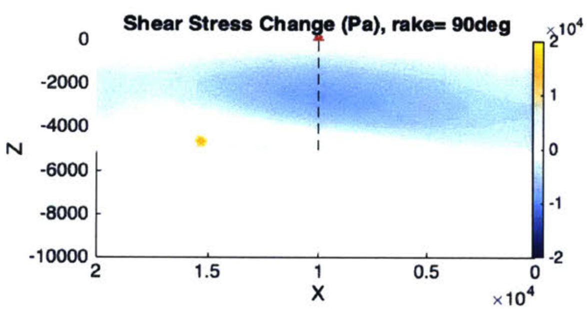

(c) UAF Shear Stress Change [Pa]

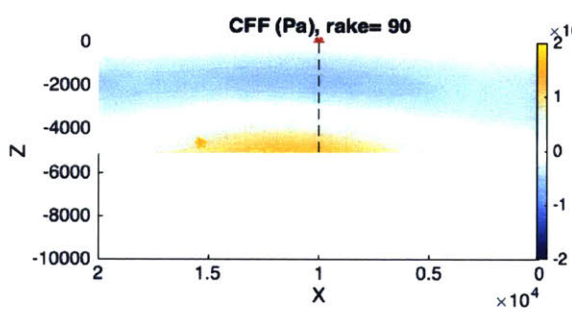

(d) UAF ΔCFF [Pa]

Figure 4-10: 3D Poroelastic Results for UAF with 90° Rake

The stress changes were exported for a line on each fault. The location of the line is where the bisecting cut (Figure 4-3) intersects with the fault. It is shown by the dashed line in Figures 4-10 and 4-9. The stress changes for the AMF can be seen in Figure 4-11, and for the UAF in Figure 4-12. As seen above, the AMF is entirely stabilized (ΔCFF<0). The maximum magnitude of the ΔCFF is -0.13 MPa. In contrast, the UAF is destabilized below 4 km, with a maximum ΔCFF of 0.027 MPa.

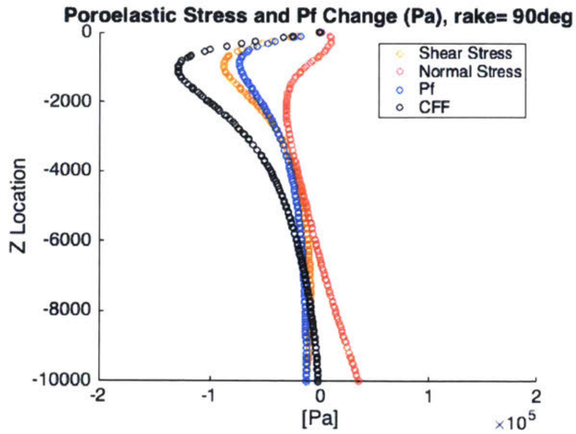

Figure 4-11: Line Plot Poroelastic Results for AMF with 90° Rake [Pa]

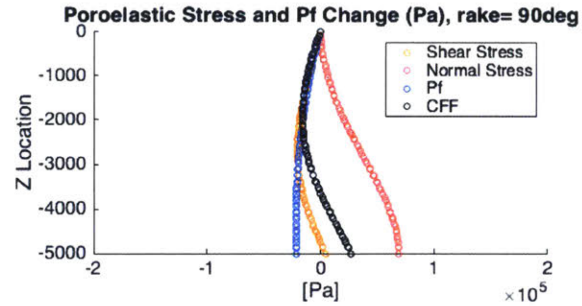

Figure 4-12: Line Plot Poroelastic Results for UAF with 90° Rake [Pa]

4.2.3.2 The Affect of Rake on Stress Changes

As seen in Chapter 2, the rake was very poorly defined for the 2011 Earthquake. Estimates ranged from 36° to 77°, using the Aki-Richards convention (Chapter 1). Due to this uncertainty, the models were run with a rake of from 0° (left lateral), 45° (oblique) and 90° (reverse). As expected, it can be seen in Figure 4-13 that the rake significantly affected the stress patterns.

It can immediately be seen that the AMF plane (Figures 4-13a, 4-13c and 4-13e) became *stabilized* almost everywhere due to the extraction of the aquifer, independent of the rake. This is an important result, and directly contrasts to the results by Gonzalez *et al.*, where it was proposed that the extraction of the Alto Guadalentín Basin may have triggered the fault slip on the AMF [6]. Moreover, the results from COMSOL agree with the updated poroelastic results by Jha *et al.* [10].

The results from the UAF are more variable depending on the rake. For the ΔCFF for a rake of 0°, or left lateral slip, the fault is stabilized on the left hand side (NE) and destabilized on the right hand side (SW). Even though the location and depth is not perfectly constrained, the general epicenter relative to Lorca is consisent. There is confidence that the 2011 Earthquake occured at $\sim x$=1.5km, which is directly in the zone of stabilization. This is an interesting result since the AMF system has predominately left lateral motion [4]. This indicates that on both the AMF and UAF

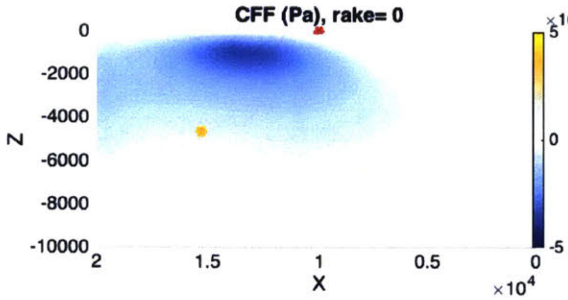

(a) 3D Poroelastic ΔCFF Results for AMF with 0° Rake [Pa]

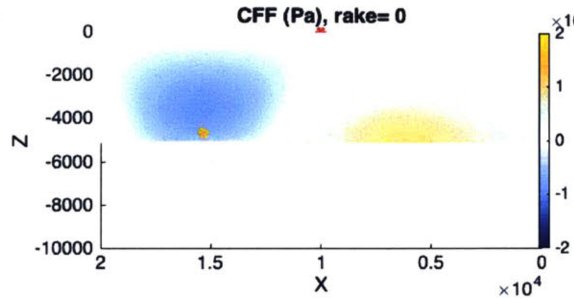

(b) 3D Poroelastic ΔCFF Results for UAF with 0° Rake [Pa]

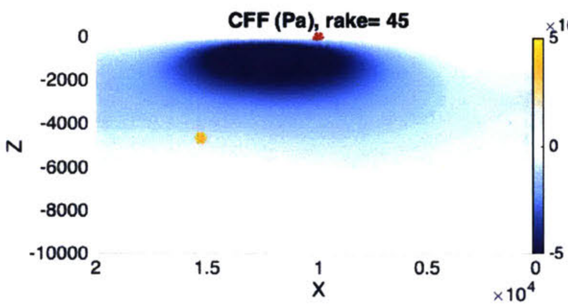

(c) 3D Poroelastic ΔCFF Results for AMF with 45° Rake [Pa]

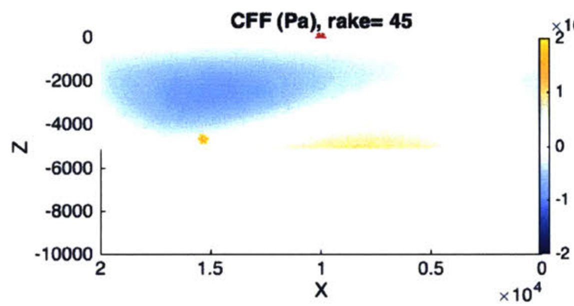

(d) 3D Poroelastic ΔCFF Results for UAF with 45° Rake [Pa]

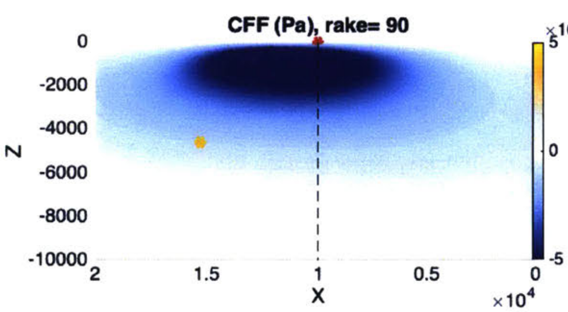

(e) 3D Poroelastic ΔCFF Results for AMF with 90° Rake [Pa]

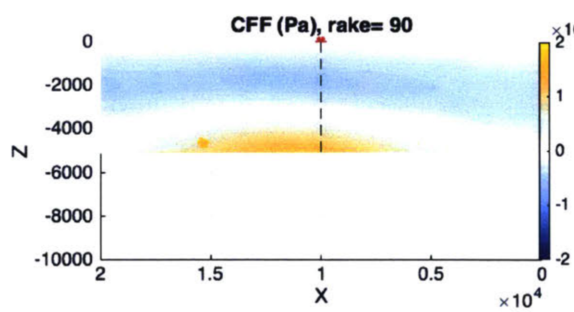

(f) 3D Poroelastic ΔCFF Results for UAF with 90° Rake [Pa]

Figure 4-13: 3D Poroelastic ΔCFF for Various Rakes (0°, 45°, 90°) for the AMF and UAF Systems faults, the left lateral motion near the hypocenter of the 2011 earthquake is *stabilized* by the extraction of the aquifer.

At a rake of 45°, the trends begin to change. The zone of destabilization moves more toward the $x+$ direction. Many of the published rakes are in the range of 45°-90°, so this is within the zone of interest. At 90°, the hypocenter is well within the zone of instability. The dashed line in Figures 4-13e and 4-13f are the plotting locations for the line plots (Figures 4-11 and 4-12). At that particular (x, y) location, the plane enters the zone of instability at ~4 km depth. There is a maximum ΔCFF of 0.027 MPa (0.27 bar), which is a small, but not insignificant, stress change.

These results draw an interesting conclusion about the source of the 2011 Lorca earthquake. Due to the small stress changes from the poroelastic results, it must be assumed that the ruptured fault was already on the verge of failure. From the FEM results, it is then concluded that the extraction of water from the Alto Guadalentín Basin decreased the probability of failure on the AMF and increased the probability of a reverse slip on the UAF. However, the contributed stress change was only ≈0.03 MPa and the total stress drop is approximately to be ≈2 MPa. The contributed changes on the UAF were only ≈1% of the total stress change.

The important conclusion from this project is that the poroelastic deflation of an aquifer does have the potential to cause a destabilization of a pre-existing fault. However, these results are dependent on the fault parameters like dip, location and strike. Additionally, the stress change pattern is dependent on the aquifer size, permeability and Young's Modulus of the solid.

4.2.3.3 Subsidence

To compare to field results, the hydraulic head and vertical displacement at the surface (z=0) were analyzed (Figures 4-14 and 4-15). As expected from a linear storage model, the subsidence increases at the same rate as the change in hydraulic head. The negative vertical displacement confirms that the aquifer is contracting as expected. However, the total vertical displacement over 50 years is 0.8 m, which is smaller than the observed result of ~10 cm/yr.

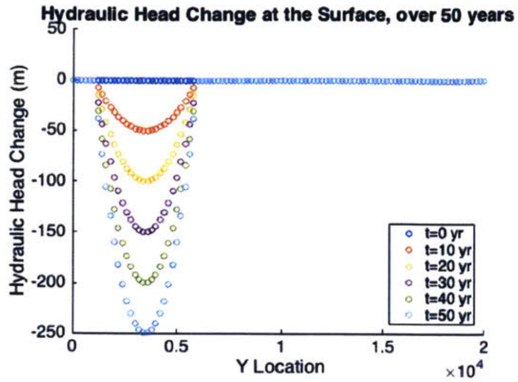

Figure 4-14: Lorca Aquifer Hydraulic Head Change from Model

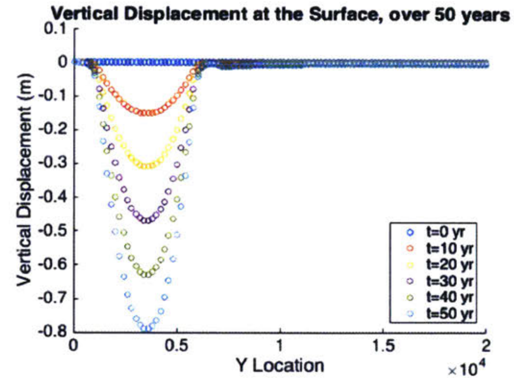

Figure 4-15: Lorca Aquifer Subsidence from Model

The less than observed subsidence of the aquifer provides some indication that the modeled results are not properly replicating the field results. There could be some explanations for this discrepancy. For example, the aquifer is likely not fully elastic and the inelastic properties of the aquifer may be important to consider [14]. If the compaction was irreversible on some time scales, this would add an interesting complexity to the problem. In the field, the volumetric strain of the aquifer may not respond fully to the pore pressure changes. Additionally, this discrepancy in the subsidence may indicate that the Young's Modulus or porosity values are incorrect.

4.2.4 Comparison of COMSOL Poroelastic and Elastic Models

Since the elastic model did not have a program like Coulomb 3.4 for comparison, the individual stress changes were analyzed to ensure that the results aligned with expectations. The stress changes for $\Delta\sigma_{xx}$, $\Delta\sigma_{yy}$ and $\Delta\sigma_{zz}$ are displayed here.

It can be seen that, in general, the aquifer causes an extension on the AMF. Looking at $\Delta\sigma_{yy}$ in Figure 4-16b, the pull is concentrated in the middle (x=1000 m), and tapers out toward the edges. The extension is also large for $\Delta\sigma_{xx}$ in Figure 4-16a toward $x+$. This is correlated with the fault curving toward the aquifer. It appears that to a simple approximation, far from the aquifer, the unloading stress is acting to 'pull' on the fault. Toward the top of the model (z=0), it seems that the Poisson

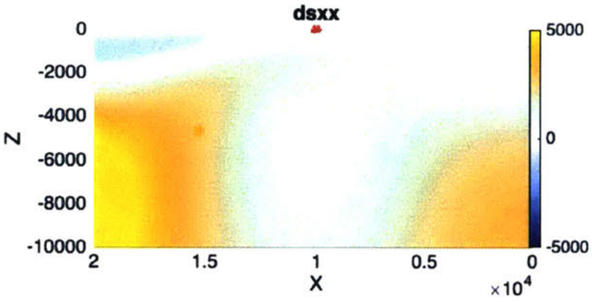

(a) AMF Elastic $\Delta\sigma_{xx}$ [Pa]

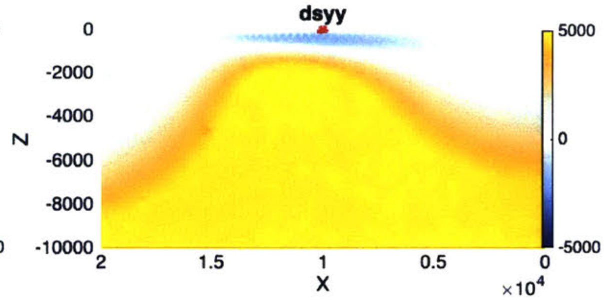

(b) AMF Elastic $\Delta\sigma_{yy}$ [Pa]

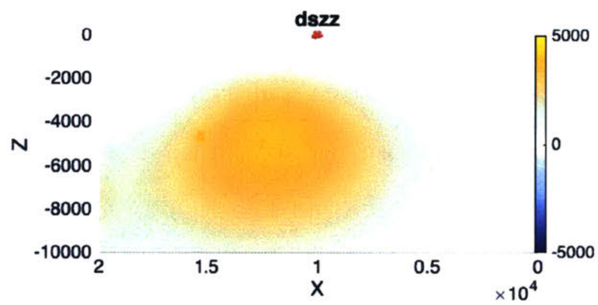

(c) AMF Elastic $\Delta\sigma_{zz}$ [Pa]

Figure 4-16: 3D Elastic Total Stress Changes ($\Delta\sigma_{xx}$, $\Delta\sigma_{yy}$, $\Delta\sigma_{zz}$) for the AMF

effect is present and the elastic solid is contracting in response to the extension caused by the upward boundary load. As a first pass, it seems that these plots agree with intuition for the application of an unloading gravitational stress.

Now, the figures will refer back to the ΔCFF, $\Delta\sigma_n$ and $\Delta\tau$ plots. The COMSOL elastic model was then run and compared with the full poroelastic model. Figure 4-17 depicts the stress changes for the standard line on the AMF, with a rake of 90°. It can be seen that the stress changes are smaller than in the full poroelastic case. In the elastic case, the ΔCFF is $\approx$2.5 kPa, and the poroelastic case is $\approx$20 kPa.

Next, the model was re-run with with various rakes. Figure 4-18 depicts the elastic stress changes on the face of the fault. This figure can be directly compared to

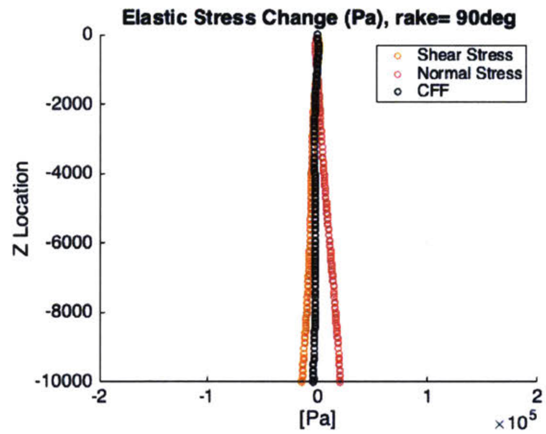

Figure 4-17: Line Plot Elastic Results for AMF with 90° Rake [Pa]

the poroelastic version in Figures 4-13a, 4-13c, 4-13e. By comparing the poroelastic results, it can be seen that the poroelastic results have a significantly higher magnitude of stress change. Additionally, more notably, the stress patterns are significantly different. For the Lorca project, the full poroelastic model includes both the deflating aquifer and also the unloading gravitational stresses. The elastic model includes only the unloading stresses.

Figure 4-18b (rake=36°) is displayed to be able to compare to the results of González *et al.* Recall that in the COMSOL setup, the NE is toward the left hand side of the image, which is opposite to what is seen in the González *et al.* paper. It can be noted that although the stress change magnitudes are similar, the stress patterns are significantly different. The reason for this has not yet been explored, but it is an important question to ask. The unloading effect, although small, does change the resulting stress pattern. The intention of this project was not to remodel the results of González *et al.*, so it is possible that there are some parameter differences in the models. However, on inspection, the results of González *et al.* are surprising.

This discussion will refer to the total stress images in Figure 4-16. For a first order and simplified approximation, the unloading stress is as if the water extraction is causing a pull on the fault toward the aquifer. For a rake of 36°, there is a dominant left lateral and reverse movement to the slip. With this in mind, the González *et al.* ΔCFF Model is surprising. If the unloading stress is causing a pull toward the

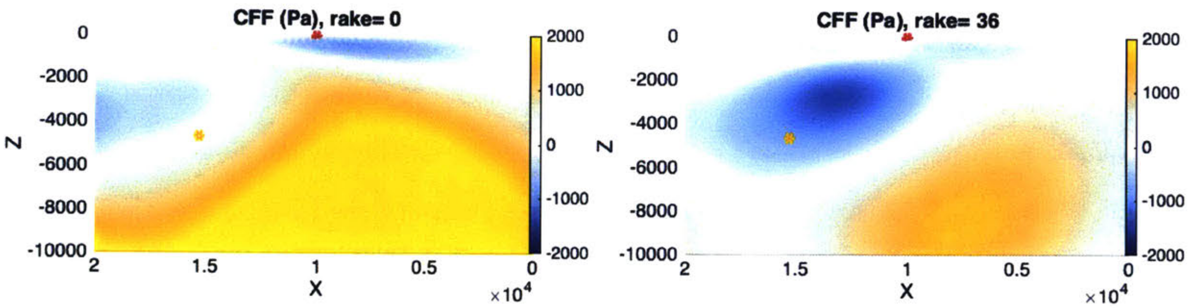

(a) 3D Elastic ΔCFF, AMF with 0° Rake (b) 3D Elastic ΔCFF, AMF with 36° Rake

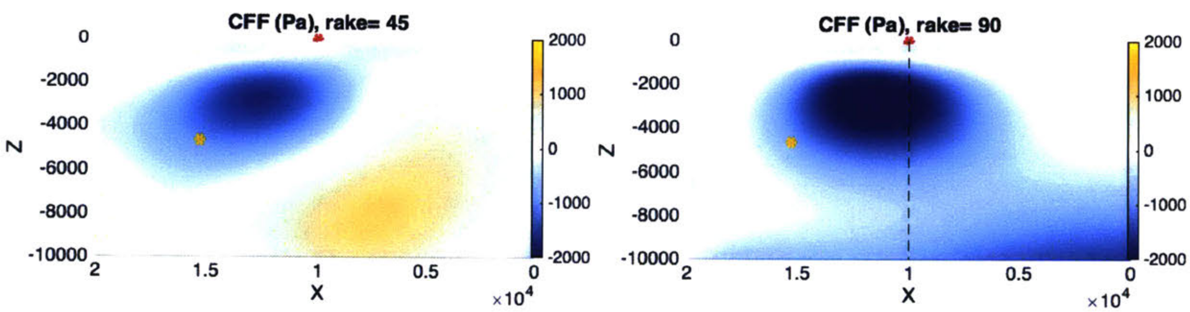

(c) 3D Elastic ΔCFF, AMF with 45° Rake (d) 3D Elastic ΔCFF, AMF with 90° Rake

Figure 4-18: 3D Elastic ΔCFF for Various Rakes (0°, 45°, 90°) for the AMF and UAF Systems [Pa]

aquifer, it would be expected that on the northern segment of the AMF, where the hypocenter is located, that *right-lateral* and *normal* movement is promoted. This would result in a negative ΔCFF in the region near the hypocenter, which agrees with the COMSOL results and disagrees with the González *et al.* results. However, it is emphasized that this is a simplified approximation and there may be another affect that is causing the positive ΔCFF in González *et al.*'s results. To understand the published results better, it would be important to see the shear and normal stress changes. The discrepancy has not yet been fully understood.

4.3 Conclusion

From the COMSOL and MATLAB results, it appears that the extraction of the Alto Guadalentín basin promoted failure on the UAF segment at a depth of $\sim$5km. Specifically, the left-lateral portion of the slip is stabilized, but the reverse component of the slip is destabilized. Also, from the perspective of the published literature, the InSAR and the focal mechanism locations are in agreement with the UAF plane. Additionally, the ΔCFF was $\approx$0.03 MPa but not insignificant, compared to the expected total stress drop ($\approx$2 MPa). However, this is a important result because it demonstrates that the poroelastic deformation of an aquifer can result in zones of stabilization and destabilization on pre-existing faults.

Chapter 5

Wheeler Ridge, California

The Wheeler Ridge project was an investigation on the affect of poroelasticity on fault stability in oil and gas applications. This section was designed to be a simplified replication of the oil production from Well 85-29, from April 13 1952 to July 21 1952. The pore fluid pressure and stress changes on the White Wolf Fault (WWF) were analyzed. This was not intended to be a complete analysis of the July 21 1952 Kern County WWF earthquake, but simply an investigation to the potential stress changes caused by heavy oil and gas extraction.

The Wheeler Ridge field is located near Bakersfield California, a very active region for oil and gas. In the figures below (Figure 5-1 and 5-2), the green dot represents the well of interest, Well 85-29. The white dot is the location of Well 22-15 which is an important spatial marker that will be used. The red line is the approximate strike of the WWF.

5.1 Problem Setup

The WWF and numerous wells can be seen in the cross section sketch in Figure 5-3. This image was important for determining the geometry of the model. The location of Wheeler Ridge and Well 22-15 are location markers used to determine the geometric constraints of the model.

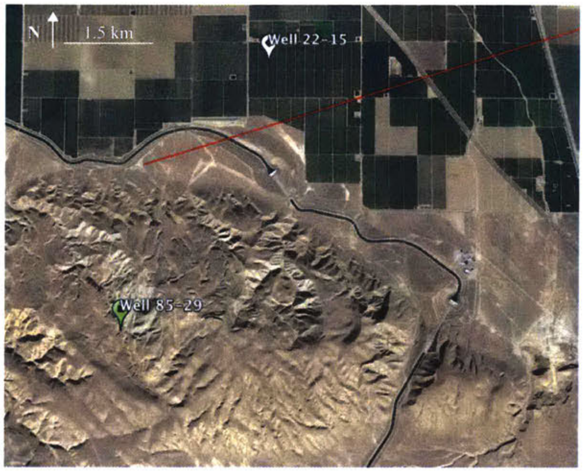

Figure 5-1: Wheeler Ridge from Google Earth

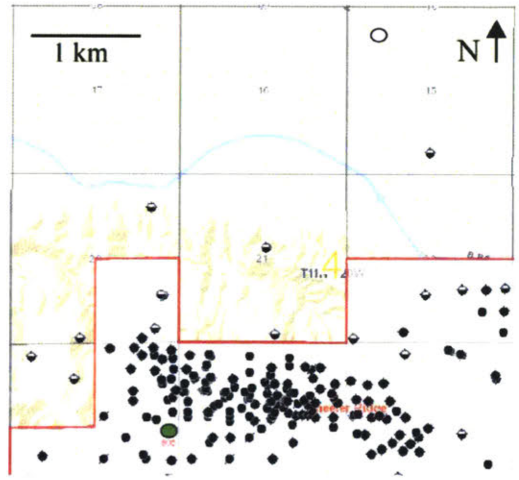

Figure 5-2: Wheeler Ridge Map View of Production Wells

5.1.0.1 Well 85-29 Data

The parameters for Well 85-29 were determined primarily from documentation provided by the USGS. The well is located in Section 29 of the Kern County field. The toe depth of the well is 9756 ft, with perforations from 9592 ft - 9756 ft. The well began producing on April 13 1952, but a leak was discovered and all production was stopped until May 14th 1952. On May 15th, May 31 and August 12 steady production rates of 419 bbl/day, 368 bbl/day and 394 bbl/day, respectively, were recorded. It was assumed that the well was producing at 400 bbl/day for appropriately 70 days. Assuming an oil density of 900 [kg/m^3], the mass flow rate was calculated to be 0.66 kg/s.

5.1.0.2 Geometry

The geometry of the model was primarily based on Figure 5-3. The z direction was assumed to be the vertical axis, with positive up. The y axis was set along the horizontal direction with positive pointing approximately from the Wheeler Ridge anticline to Well 22-15. The x axis extended out of the page. Since there are no other known spatial dimensions of the reservoir or fault, the model was assumed to be continuous in the x direction.

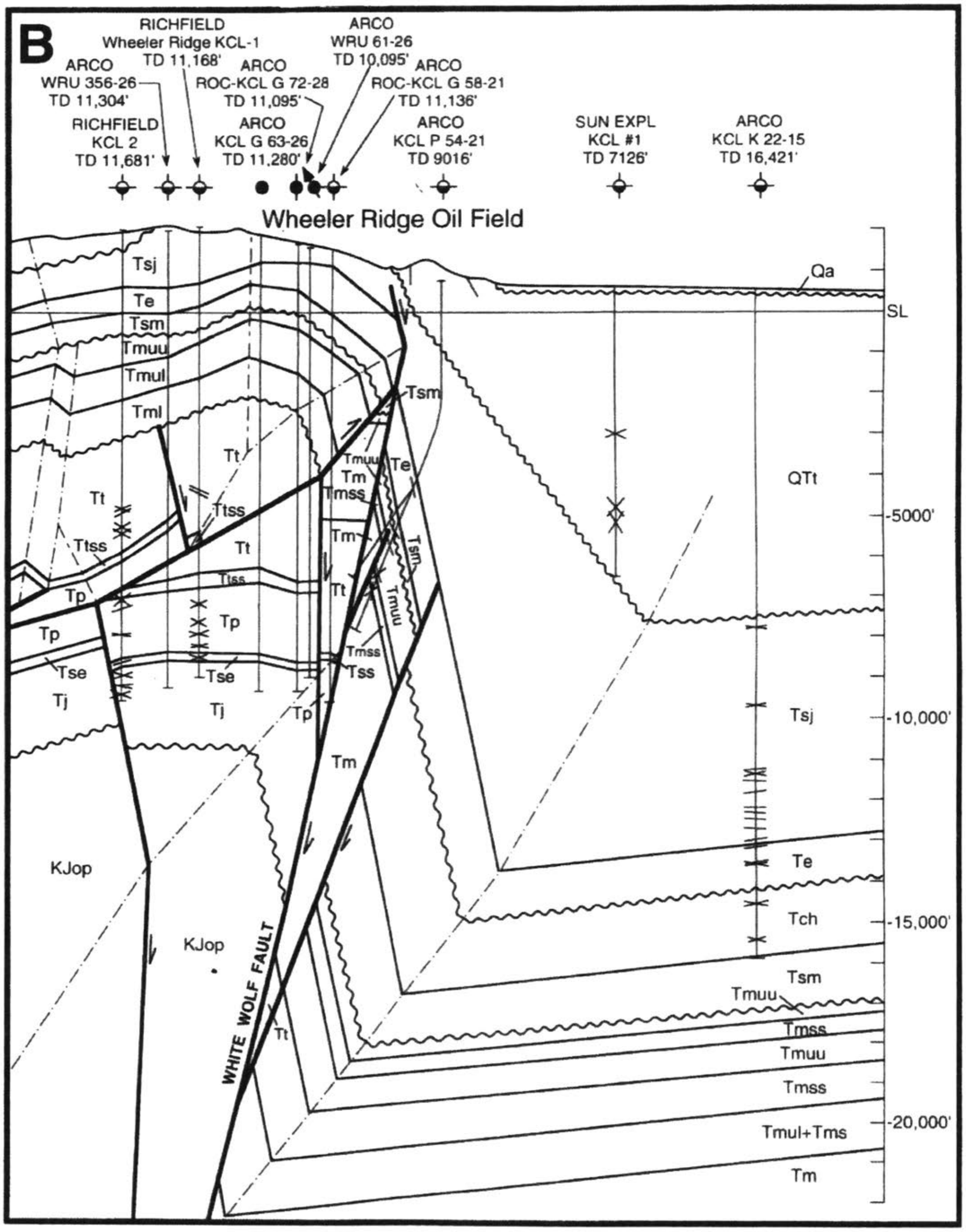

Figure 5-3: Wheeler Ridge Cross Section provided by USGS

The location of Well 85-29 is known, and is located in the same plane as the Richfield Wheeler Ridge KCL-1 Well, shown in Figure 5-3. The GPS location of both Well 85-29 and Well 22-15 were also known [25], and these two wells were used to determine a general spatial extent and scaling relation for the cross section. Since the cross section collapses many well locations onto one plane, the size of the cross section is a rough approximation. From this, a geometry of 10 km (x) x 10 km (y) x 6 km (z) was built. The area shown in the Figure is assumed to be ~4.5 km across, but room was added on the edges to avoid boundary affects. The strike of the fault was set to be in the middle of the domain at y = 5000 m.

From the perforations, the reservoir is known to have a thickness of 50 m. It appears that the reservoir is bounded by faults on the y+ and y- side, and the reservoir was assumed to be constrained in the y direction. Additionally, a gap was added between the reservoir and the fault. The model set up can be seen in Figure 5-4. and the geometry parameters are provided in Table 5.1.

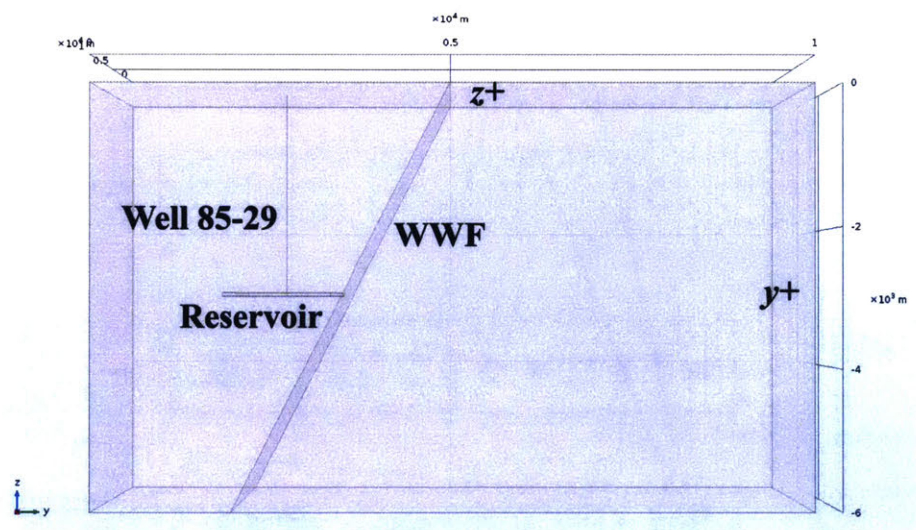

Figure 5-4: COMSOL 3D Wheeler Ridge Geometry Image

5.1.0.3 Initial Conditions and Boundary Conditions

In COMSOL, the boundary and initial conditions were entered into the appropriate sections of *Darcy's Law* and *Solid Mechanics*. The updated and Wheeler Ridge specific COMSOL interface is displayed here for reference (Figure 5-5). Note that there is no *Boundary Load* added. In this example, the oil is replaced by the water which is a smaller density change than the Lorca project where the water was replaced by air. For all other features, refer to Chapter 3 for a complete description.

Table 5.1: Wheeler Ridge Geometry

Reservoir		
	Top (z)	-2925 m
	Base (z)	-2975 m
	Length (y)	1500 m
	Edge Location (y-)	1600 m
	Edge Location (y+)	3100 m
	Width (x)	10000 m
Well		
	Location (x,y)	5000 m 2350 m
	Depth (z)	-2975 m
	Diameter	0.1 m
	Pump Rate	0.66 kg/s
Fault		
	Surface Location (y)	5000 m
	Fault Dip	63°

The initial stress condition was chosen to be lithostatic for simplicity. Additionally, the initial fluid pressure was set to be hydrostatic. This was assumed for two reasons. One, the density change between oil and water is small. Two, the true pressure of the reservoir is unknown due to the fact that hydrocarbon reservoirs are generally over-pressurized. The hydrostatic assumption was a neutral approximation. Additionally, for this application, the final pressure change was the value of interest. The initial conditions can be seen in Table 5.2.

For the *Solid Mechanics* section, the initial stress state was controlled through the *Linear Elastic Material* > *Initial Stress* and The *Linear Elastic Material* > *External Stress* section. The *Initial Stress* included the σ_{ii} stresses listed in Table 5.2, and the *External Stress* included the pore fluid pressure. For the boundary conditions, the *Free* condition was applied to the top surface (z+), while the *Roller* condition was applied to all other sides (x+, x-, y+, y-, z-).

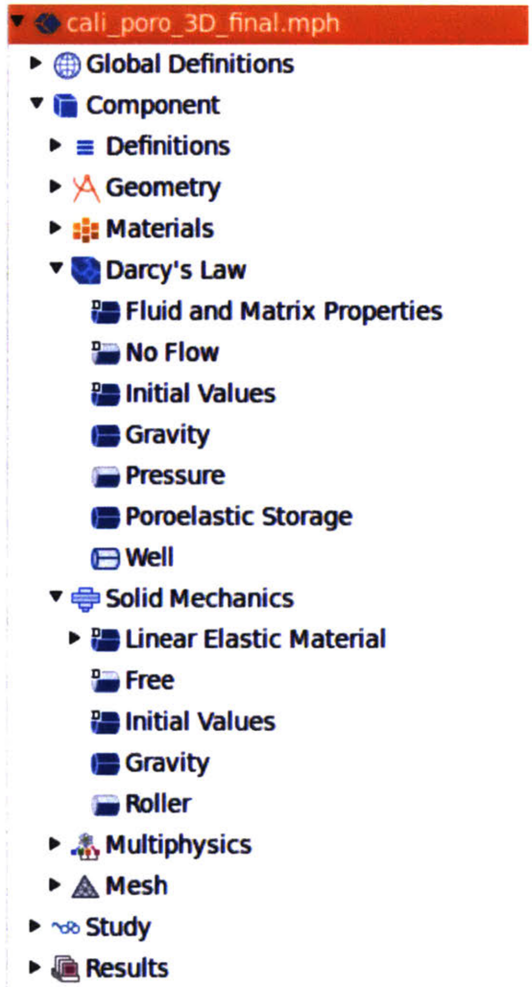

Figure 5-5: Wheeler Ridge COMSOL Interface

Table 5.2: Wheeler Ridge Initial Conditions

Stress in x, y, z direction	σ_{ii}	$-\rho_{av} g\|z\|$
Pore Pressure	p_f	$\rho_w g\|z\|$
Displacement	u, v, w	0 [m]
Strain	ε_{ij}	0

For the *Darcy's Law* boundary conditions, the *Pressure* condition was applied to the top surface ($z+$) and p_f was set to 0 Pa. The *No Flow* condition was applied to all other sides ($x+$, x-, $y+$, y-, z-). Note that all other reference pressures were also set to 0 Pa so there was no induced flow.

Finally, the time dependent factor was added to the model. COMSOL 5.3 has the ability to add a well to the model in *Darcy's Law > Well.* The well was identified as a production well, and the parameters can be seen in Table 5.1. The production was set to occur from the perforated area of the wells (2925 m - 2975 m).

For this part of the project, there was no boundary force added. In Lorca, the aquifer was a free surface and the water was being replaced with air. This decrease in density resulted in a gravitational unloading force. However, in the application with a reservoir, the oil is normally replaced with water. Since the density change is small, there was no load added to the model.

5.1.0.4 Updated COMSOL Poroelastic Equations

The final COMSOL equations were modified to account for the mass sink. The solid equation was not modified, but the Darcy flow equation was. A generic mass source term (Q) was added to represent the flux into the well.

$$-\nabla \cdot (\mathbf{C}\boldsymbol{\varepsilon} - \alpha p_f \mathbf{I}) = (\rho_f \theta + (1-\theta)\rho_s)\mathbf{g} \quad \varepsilon_{ij} = \frac{1}{2}\left(\frac{\delta u_i}{\delta x_j} + \frac{\delta u_j}{\delta x_i}\right) \tag{5.1}$$

$$S\frac{\delta p_f}{\delta t} + \nabla \cdot [-\frac{\kappa}{\mu_f}(\nabla p_f - \rho_f \mathbf{g} \nabla D)] = Q - \alpha\frac{\delta \varepsilon_{vol}}{\delta t} \tag{5.2}$$

5.1.0.5 Parameters and Variables

The parameters and variables chosen for the COMSOL aspect of the project can be seen in Table 5.3. Note that the permeability is the only variable or parameter that does not apply to the entire region. The permeability is a high value within the reservoir, but it is a constant low value everywhere else in the region. The parameters inputed for this section where chosen with the intention to make the model as simple as possible. Standard values for permeability, friction, density and porosity etc were chosen. The fault angle was approximated from literature [13]. The model was run for 70 days, replicating the pumping time of Well 85-29 before the earthquake.

Table 5.3: Wheeler Ridge General Parameters

Biot Coefficient	α	1
Coefficient of Friction	μ	0.6
Compressibility of Water	c_w	4×10^{-10} [Pa^{-1}]
Storage Coefficient	S	$\theta\ c_w$
Density of Solid	ρ_s	2600 [kg/m^3]
Density of Water	ρ_w	1000 [kg/m^3]
Density of Rock (Drained)	ρ_d	$(1\text{-}\theta)\rho_s$
Density (Average)	ρ_{avg}	$\rho_d+\theta\rho_w$
Dynamic Viscosity of Water	μ_w	1 [cP]
Permeability within Reservoir	k	10000 [mD]
Permeability outside of Reservoir	k	0.0001 [mD]
Poisson's Ratio	ν	0.25
Porosity	θ	0.1
Young's Modulus	E	$E_m z + E_b$
	E_m	-7.99 [MPa/m]
	E_b	100 [MPa]

5.2 Results and Discussion

The resulting changes from the extraction of Well 85-29 can be seen in along fault plots (Figure 5-6) and a line plot (Figure 5-7). The pore pressure change (Figure 5-6a), normal stress change (Figure 5-6b), shear stress change (5-6c) and ΔCFF (Figure 5-6d) are displayed along the WWF, with ~E on the left and ~W on the right. For simplicity, the rake was set to 90°. The documentation describes the WWF with a reverse slip with a small left lateral component, it was found that a rake modification did not have a significant affect on the stress change. It can be seen that there is distinct pattern of stabilization (blue) vs destabilization (yellow/orange) in the ΔCFF plots.

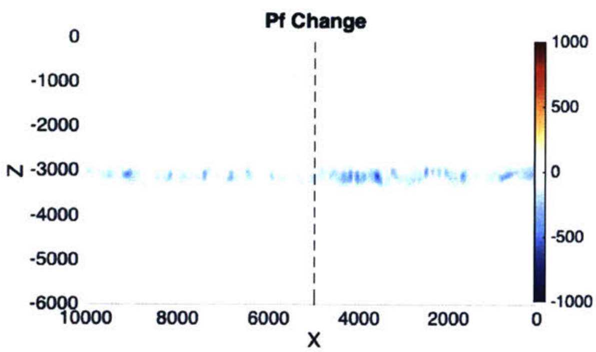

(a) WWF p_f Change [Pa]

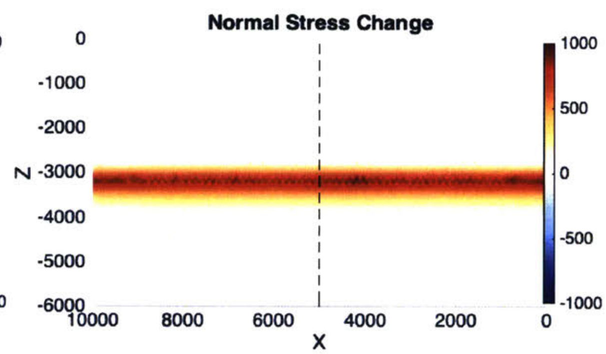

(b) WWF Normal Stress Change [Pa]

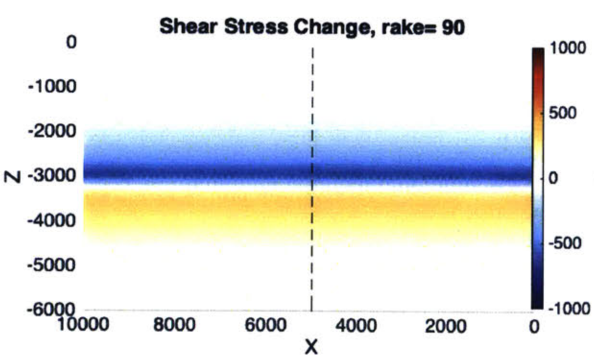

(c) WWF Shear Stress Change [Pa]

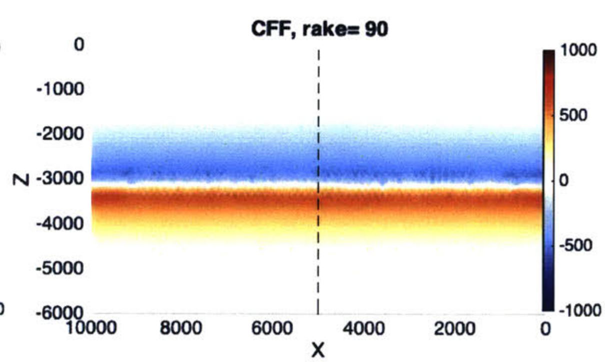

(d) WWF ΔCFF [Pa]

Figure 5-6: 3D Poroelastic Results for WWF with 90° Rake

The value of this stress change can be more closely seen in the line plot. The location of the line plot is shown by the dashed lines in Figure 5-6. The ΔCFF has a minimum value of -0.5 kPa at a depth of 2.8 km. The maximum ΔCFF is 0.7 kPa at 3.3 km. Also, it is interesting to note that pore fluid pressure change is ≈0. This was assumed to be because of the short run time of the model (70 days). The stress changes are significantly lower than the values determined in the Lorca project.

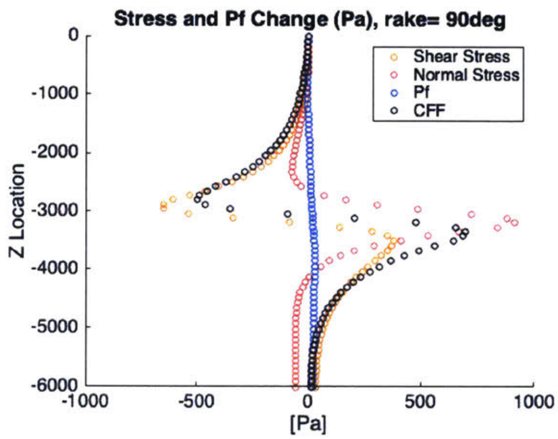

Figure 5-7: Line Plot Poroelastic Results for WWF with 90° Rake [Pa]

Some parameters were varied to understand the effect on the magnitude of the stress change. Figure 5-8 depicts a decrease in permeability to k=100 mD (from 10000 mD). These permeabilities represent the high and low end members for oil and reservoirs. Figure 5-9 depicts an change in width of the permeable reservoir, to 5 km (from 10 km).

The permeability of the reservoir was decreased by two orders of magnitude. However, this had no noticeable effect on the stress and pore pressure changes. Next, the width of the aquifer was changed to be 5 km, from 10 km. Notice the change of the scale bar in Figure 5-9. As the width was halved, the stress change increased by a factor of 2. It appears that there is a linear relationship between the area being extracted and the stress changes on the fault. Neither the permeability or the width significantly change the results. Even when increased by a factor of two, this stress change is significantly smaller than expected for it to have an effect on the triggering of an earthquake. The expected stress change is ~0.1-1 MPa.

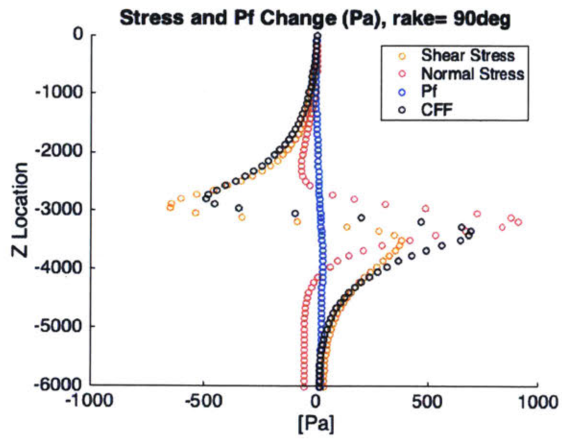

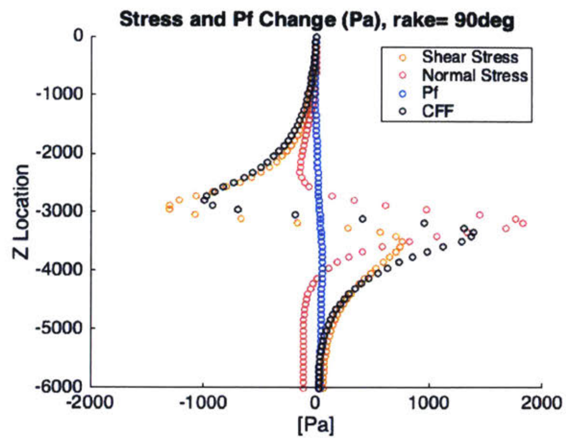

Figure 5-8: Line Plot for WWF with k=100 mD [Pa]

Figure 5-9: Line Plot for WWF with Reservoir Width 5000 m [Pa]

Additionally, another consideration is any updates to the Solid Mechanics equation. Recall that the right hand side of Equation 5.1 is assumed to be a constant, even if the porosity and densities change. In the Wheeler Ridge project, it is assumed that the density change of the fluid is small as the oil (900 kg/m^3) is replaced with water (1000 kg/m^3). However, the porosity of the reservoir is changing as the mass is being extracted. However, a calculation for this was completed assuming that $\delta\varepsilon_{vol}$ was equivalent to the porosity change, and the effect was found to be negligible.

5.3 Conclusion

Looking at the stress distribution, it is interesting to note that the region adjacent to but below the aquifer tends toward destabilization. Well 85-29 was the first deep well that was drilled in this area, and would have been the first well that could have had an affect on this deeper region of the WWF. This may fit the hypothesis that Well 85-29 enabled the nucleation of an earthquake in a way that the previously drilled shallow wells in the surrounding area could not have. Additionally, there are other unique factors of the 1952 slip [13]. First, the WWF trends NE, which is opposite to the other major faults in the area that have had major earthquakes. Most other major earthquakes have occurred on faults trending NW, aligned with the San Andreas.

Second, slip was reverse with a minor left lateral component. Most other earthquakes in the area are right lateral. The discrepancy between the 1952 earthquake and other earthquakes in the area suggests that the initiation may have been different. This supports the hypothesis of the triggering from the oil extraction.

However, the very small stress change caused by the producing well is a draw back on this conclusion. From the COMSOL-MATLAB results, there is a notably small stress change ($\approx$0.5 kPA). For a future project, it would be interesting to do a more complete analysis of all of the wells pumped in the Wheeler Ridge area. Since there is a strong time dependence on the ΔCFF, it may be important to consider more of the wells in the Wheeler Ridge area. The first successful well was drilled in 1922, and it was a very prolific site up to and past 1952. However, since these wells are highly spatially distributed, the problem would quickly become very geologically complex.

Bibliography

[1] Wang, H. F. (2000). Introduction, *Theory of Linear Poroelasticity with Applications to Geomechanics and Hydrogeology* (pp. 3-25). Princeton, New Jersey: Princeton University Press.

[2] King, N. E., et al. (2007), Space geodetic observation of expansion of the San Gabriel Valley, California, aquifer system, during heavy rainfall in winter 2004–2005, *Journal of Geophysical Research, 112*, B03409, doi:10.1029/2006JB004448

[3] USGS Software. (n.d.). *Coulomb 3.3 User Guide*, Retrieved from `https://earthquake.usgs.gov/research/software/coulomb/`

[4] Martínez-Díaz, J.J., Masana, E. & Ortuño, M (2012). Active Tectonics of the Alhama de Murcia Fault, Betic Cordillera, Spain. *Journal of Iberian Geology, 38*(1), pp. 253-270, `http://dx.doi.org/10.5209/rev_JIGE.2012.v38.n1.39218`

[5] López-Comino, J., Mancilla, F., Morales, J. & Stich, D. (2012). Rupture Directivity of the 2011, Mw 5.2 Lorca Earthquake (Spain). *Geophysical Research Letters, 39*, L03301, doi: 10.1029/2011GL050498

[6] González, P. J., Tiampo, K. F., Palano, M., Cannavo, F. & Fernández, J. (2012). The 2011 Lorca Earthquake Slip Distribution Controlled by Groundwater Crustal Unloading. *Nature Geoscience Letters, 5*, pp 821-825. doi: 10.1038/NGEO1610

[7] González, P. J., Tiampo, K. F., Palano, M., Cannavo, F. & Fernández, J. (2012). The 2011 Lorca Earthquake Slip Distribution Controlled by Groundwater Crustal Unloading. *Nature Geoscience Supplementary Information*, doi: 10.1038/NGEO1610

[8] Jha, B. (2014). Flow Through Porous Media: From Mixing of Fluids to Triggering of Earthquakes (Doctoral dissertation). Massachusetts Institute of Technology, Cambridge, Massachusetts.

[9] Jha, B. & Juanes, R. (2014). Coupled Multiphase Flow and Poromechanics: a Computational Model of Pore Pressure Effects on Fault Slip and Earthquake Triggering. *AGU Publications Water Resources Research.* doi: 10.1002/2013WR015175.

[10] Jha, B., Hager, B. & Juanes, R. (n.d.). *Coupled Flow and Geomechanical Analysis of the 2011 Lorca Earthquake.* Poster.

[11] Carls, J. M., (1951). Recent Developments in Wheeler Ridge Oil Field, *Summary of Operations - Oil Fields, Division of Oil and Gas* (pp. 20-24). Provided by the USGS.

[12] Wheeler Ridge, (n.d.) *Summary of Operations - Oil Fields, Division of Oil and Gas* (pp. 20-24). Provided by the USGS.

[13] State of California Department of Natural Resources Division of Mines (1955). *Earthquakes in Kern County, California During 1952 (Bulletin 171).* San Francisco, California.

[14] González, P. J. & Fernández, J. (2011). Drought-Driven Transient Aquifer Compaction Imaged Using Multitemporal Satellite Radar Interferometry. *Geology, 39*(6), pp. 551-554. doi: 10.1130/G31900.1

[15] De Michelle, M., Briole, P., Raucoules, D., Lomoine, A. & RIGO, A. (2013). Revisiting the Shallow M_w 5.1 Lorca Earthquake (Southeastern Spain) using C-Band InSAR and Elastic Dislocation Modeling. *Remote Sensing Letters, 4*(9), pp. 863–872. `http://dx.doi.org/10.1080/2150704X.2013.808777`

[16] Pro, C., Buforn E., Cesca S., Sanz De Galdeano, C. & Udías, A (2014). Rupture Process of the Lorca (southeast Spain) 11 May 2011 (M_w=5.1) Earthquake. *Journal of Seismology 18*, pp. 481-95. doi: L10.1007/s10950-014-9421-8

[17] Stich, D., R. Martin & Morales, J. (2010), Moment tensor inversion for Iberia-Maghreb earthquakes 2005–2008, *Tectonophysics, 483*, pp. 390–398, doi:10.1016/j.tecto.2009.11.006

[18] Bousquet, J. C. (1979), Quaternary strike-slip faults in southeastern Spain, *Tectonophysics, 52*, pp. 277–286, doi:10.1016/0040-1951(79)90232-4

[19] COMSOL Software 5.3 (n.d.). *Terzaghi Compaction*, Retrieved from `https://www.comsol.com/model/terzaghi-compaction-491`

[20] COMSOL Software 5.3 (n.d.). *Biot Poroelasticity*, Retrieved from `https://www.comsol.com/model/biot-poroelasticity-483`

[21] COMSOL Software 5.3 (2017). Theory for the Poroelasticity Interface. *Subsurface Flow Module User's Guide* (pp. 214-217)

[22] Okada, Y. (1992) Internal Deformation Due to Shear and Tensile Faults in a Half-Space. *Bulletin of the Seismological Society of America, 82*(2), pp. 1018-1040.

[23] Fang, M. (n.d.). *Solutions for the Hager's Demo-Model.*

[24] Cerón, J. C. & Pulido-Bosch, A. (1996). Groundwater Problems Resulting from CO_2 Pollution and Overexploitation in Alto Guadalentin Aquifer (Murcia, Spain). *Environmental Geology, 28*(4), pp. 223-228.

[25] Drilling Edge (n.d.). Retrieved June 22, 2017, from `www.drillingedge.com`